Steel TIPS
STRUCTURAL STEEL EDUCATIONAL COUNCIL
TECHNICAL INFORMATION & PRODUCT SERVICE

August 2006

# *Buckling and Fracture of Concentric Braces Under Inelastic Cyclic Loading*

By

**Benjamin V. Fell**
Graduate Research Assistant
University of California at Davis

**Amit M. Kanvinde**
Assistant Professor
University of California at Davis

**Gregory G. Deierlein**
Professor, Director of John A. Blume Earthquake Engineering Center
Stanford University

**Andrew T. Myers**
Graduate Research Assistant
Stanford University

**Xiangyang Fu**
Graduate Research Assistant
University of California at Davis

## Buckling and fracture of concentric braces under inelastic cyclic loading

By Benjamin V. Fell, Amit M. Kanvinde, Gregory G. Deierlein, Andrew T. Myers, Xiangyang Fu

Experimental findings and design implications from nineteen tests of large-scale concentric steel braces are presented. Rectangular hollow structural sections (HSS), round pipe, and W-shape cross sections of varying width-thickness and slenderness ratios are subjected to various loading histories. Ductile fracture during inelastic cyclic buckling is found to be driven by strain amplification due to local buckling of the cross section. Cross section shape, width-thickness ratio, and brace slenderness ratio are the most important factors that control brace ductility. Pipe and wide-flange shapes are observed to be more resilient to fracture as compared to HSS members that develop large local buckling induced strains at the corners. Parameters that have less significant effect on buckling and fracture response include concrete filling of HSS members and loading rates. The relatively low displacement ductility of the HSS members suggests the need to reduce the permissible section width-thickness requirements for seismic design. Tests with and without reinforcing at the slotted HSS and pipe to gusset plate connections demonstrate the effectiveness of the reinforcing plates to prevent premature net-section fracture. The maximum brace resistance is found to be bracketed between the calculated expected yield strength ($R_yF_yA_g$) and expected ultimate strength ($R_tF_uA_g$), using nominal values specified in design specifications. Micromechanics-based models to simulate ductile fracture are introduced that can generalize the findings of this research through detailed finite element analyses.

Benjamin V. Fell, Graduate Research Assistant, University of California at Davis
bvfell@ucdavis.edu

Amit M. Kanvinde, Ph.D., Assistant Professor, University of California at Davis
kanvinde@ucdavis.edu

Gregory G. Deierlein, Ph.D., P.E., Professor, Stanford University
ggd@stanford.edu

Andrew T. Myers, Graduate Research Assistant, Stanford University
atmyers@stanford.edu

Xiangyang Fu, Graduate Research Assistant, University of California at Davis
xfu@ucdavis.edu

# ACKNOWLEDGMENTS

The publication of this report was made possible in part by the support of the Structural Steel Educational Council (SSEC). The nineteen brace specimens were donated through the SSEC and their support is greatly appreciated. The authors also thank Jeff Eandi of Eandi Metal Works, Inc. for high-quality fabrication of the specimens.

This research is supported by the National Science Foundation (NSF Grant CMS 0421492), the George E. Brown Jr. Network for Earthquake Engineering Simulation (NEES), and the Structural Steel Educational Council (SSEC). The advice and guidance of Helmut Krawinkler (Stanford University), Stephen Mahin (University of California at Berkeley), Charles Roeder (University of Washington), Walterio López and Mark Saunders (Rutherford and Chekene) is greatly appreciated. In addition, the knowledgeable support of the UC Berkeley NEES lab personnel including Shakhzod Takhirov, Donald Patterson, Donald Clyde, David MacLam, and Jose Robles greatly assisted in the experimental aspect of this study. The authors also acknowledge support from the John A. Blume Earthquake Engineering Center at Stanford University and the University of California at Davis.

Finally, the authors wish to thank SSEC members Walterio López, S.E., Michael Cochran, S.E., and Fred Breismeister, P.E. for their technical input and review of this report.

 

# TABLE OF CONTENTS

ABSTRACT / Page 2

ACKNOWLEDGMENTS / Page 3

TABLE OF CONTENTS / Page 4

NOTATIONS / Page 5

CHAPTER 1. INTRODUCTION/ Page 7

CHAPTER 2. SUMMARY OF EXPERIMENTAL PROGRAM / Page 10

CHAPTER 3. INTRODUCTION TO CONTINUUM-BASED
FRACTURE AND FATIGUE PREDICTIVE MODELS / Page 29

CHAPTER 4. DESIGN IMPLICATIONS / Page 34

CHAPTER 5. SUMMARY / Page 51

APPENDIX A. MATERIAL PROPERTIES / Page 53

APPENDIX B. EXPERIMENTAL HYSTERETIC PLOTS AND BACKBONE CURVES / Page 56

REFERENCES/Page 67

ABOUT THE AUTHOR(S) / Page 70

LIST OF PUBLISHED “STEEL TIPS” REPORTS / Page 72

# Notations

$A_g$ Gross cross sectional area, $in^2$
$A_n$ Net cross sectional area, $in^2$
$C_d$ Deflection amplification factor
$D$ Diameter of PipeSTD section, in
$E$ Modulus of elasticity of steel, E = 29,000 ksi
$F_y$ Minimum specified yield stress of steel (AISC, 2001), ksi
$F_{cr}$ Critical buckling stress, ksi
$F_{cr\text{-}Ry}$ Critical buckling stress with $R_yF_y$ amplification, ksi
$F_u$ Maximum specified ultimate stress of steel (AISC, 2001), ksi
$K$ Effective length factor
$K_{e(c)}$ Calculated elastic stiffness, k/in
$K_{e(m)}$ Experimentally measured elastic stiffness, k/in
$L_B$ Brace length, in
$M_p$ Nominal plastic flexural strength, k-in
$P_{2\%}$ Maximum experimentally measured tensile force at 2% drift, kips
$P_c$ Compression backbone estimate, kips
$P_{c,max}$ Maximum experimentally measured compressive force, kips
$P_{cr,exp}$ Expected compression strength, kips
$P_{max}$ Maximum experimentally measured tensile force, kips
$P_n$ Nominal axial strength of a compression member, kips
$P_t$ Tension backbone estimate, kips
$P_{u,exp}$ Expected ultimate strength, kips
$P_{y,exp}$ Expected yield strength, kips
$R$ Average micovoid size
$R$ Seismic response modification coefficient
$R_0$ Initial average micovoid size
$R_t$ Ratio of expected ultimate strength to the minimum specified ultimate strength, $F_u$
$R_y$ Ratio of expected yield strength to the minimum specified yield strength, $F_y$
$T$ Triaxiality, $T = \sigma_m/\sigma_e$
$U$ Joint efficiency factor accounting for shear-lag
$Z$ Plastic section modulus, $in^3$
$b$ Width of square HSS, in
$b_f$ Width of flange, in
$e^P$ Equivalent plastic strain, $e^P = \int_0^t \sqrt{\frac{2}{3}\varepsilon_{ij}^p \cdot \varepsilon_{ij}^p}\, dt$
$f'_c$ Specified compressive stress of concrete, ksi
$n$ Hardening coefficient
$r$ Governing radius of gyration, in.
$t$ Wall thickness of HSS or PipeSTD cross section, in

$t_f$ Thickness of flange, in
$\Delta_0$ Initial imperfection of an axial strut, in
$\Delta_a$ Brace axial deformation, in
$\Delta_n$ Critical buckling axial displacement, in
$\Sigma\theta_p$ Cumulative plastic drift, radians
$\alpha$ $R_y$ amplification factor
$\beta$ Angle between the horizontal plane and bracing member, degrees
$\delta$ Lateral displacement of a buckling member, in
$\varepsilon^P$ Plastic strain, in/in
$\dot{\varepsilon}$ Strain rate, $s^{-1}$
$\lambda$ Slenderness parameter
$\lambda_{cyclic}$ Damage coefficient for ULCF fracture model
$\varepsilon_F$ Strain at fracture, in/in
$\phi$ Resistance factor
$\eta$ Monotonic toughness parameter for fracture model
$\eta_{cyclic}$ Cyclic toughness parameter for ULCF fracture model
$\theta$ Story drift angle, radians
$\theta_{c,\,max}$ Maximum critical buckling drift, radians
$\theta_y$ Story drift at first yield, radians
$\theta_{MCE}$ Story drift at Maximum Considered Event (MCE) level, radians
$\sigma_e$ Effective or von Mises stress, ksi
$\sigma_m$ Mean or hydrostatic stress, $\sigma_m = \frac{1}{3}(\sigma_1 + \sigma_2 + \sigma_3)$, ksi
$\psi$ Triaxiality amplification factor in ULCF fracture model

# 1. Introduction

While concentrically braced frames are one of the more popular lateral load resisting structural systems for steel buildings in seismically active regions, they are known to be vulnerable to brace buckling and fracture. As shown in Figure 1.1, recent testing (Uriz and Mahin, 2004) has demonstrated the likelihood of ductile fracture that is induced by overall flexural brace buckling followed by concentrated local buckling. Connections between the braces and the frame are also prone to fracture; however, provisions are in place to mitigate this through connection detailing that accommodates brace end rotations and avoids net section fractures. Nevertheless, because concentrically braced frames dissipate energy through cyclic inelastic buckling of bracing elements, the resistance of braces to buckling-induced fracture may ultimately govern system ductility; and recent studies (Uriz and Mahin, 2004, Herman et al., 2006) suggest that the current AISC Seismic Provisions (2005) may not provide sufficient fracture resistance to provide the ductility implied by current building code provisions.

To address the concerns of ductile performance of bracing systems during severe ground shaking, this report is focused on the experimental performance of nineteen large-scale bracing members that were tested as part of a Network for Earthquake Engineering Simulation and Research (NEESR) project. The tests were intended to provide insights into performance of bracing elements and connections as well as to validate new fatigue and fracture modeling techniques in full-scale steel components.

Current seismic design standards (AISC, 2005) distinguish between Ordinary Concentrically Braced Frames (OCBF) and Special Concentrically Braced Frames (SCBF), where the latter have more stringent requirements to provide for larger ductility. This is reflected in the seismic response factors specified for the design of braced frames in ASCE 7 (2005). For SCBFs, ASCE 7 specifies R = 6 and $C_d$ = 5; whereas for OCBFs ASCE 7 specifies R = 5 and $C_d$ = 4.5. However, in terms of the bracing members themselves, the AISC requirements are similar for OCBFs and SCBFs, where requirements for both systems have the same limits on the brace section compactness and the brace connection design and similar limits on the overall slenderness. Therefore, the testing and results in this report are generally relevant to braces in both OCBF and SCBF systems. However, since SCBFs are preferred for regions of high seismicity, this study is presented in the context of SCBF systems, where the main practical difference is that the loading protocol is established for regions of high-seismicity assuming the larger deformation capacity of the SCBF system.

The test specimens, representing various types of SCBF braces, were subjected to reversed-cyclic loading histories to characterize their performance. The specimens are approximately two-thirds scale of brace sizes used in typical buildings and have end connections that represent the expected type of gusset plate connections used in SCBF systems. The gusset plate connections are designed in accordance with the Seismic Provisions (AISC, 2005) to ensure the formation of a yield line to accommodate rotations associated with brace buckling. The cross sections investigated in this study included two square hollow structural sections (HSS4x4x1/4

and HSS4x4x3/8), two standard pipe sections (Pipe3STD and Pipe5STD), and one wide-flange section (W12x16). The HSS and PipeSTD sections provide a variety of width-thickness and slenderness ratios within the AISC (2005) limits, while the W12x16 exceeds both the section compactness and slenderness limits for SCBF braces. In addition to width-thickness, slenderness and cross sections, the tests examine various other factors including loading histories, loading rates, connection details, and concrete fill in the HSS members. These result in key observations regarding the performance of these braces and connections that are of immediate relevance to the professional practice engaged in SCBF design.

Apart from their immediate practical relevance to seismic design, the brace tests provide high-quality data to validate the accuracy of a new type of micromechanics-based Ultra Low Cycle Fatigue (ULCF) model developed by the authors (Kanvinde and Deierlein, 2004). The validation of this model is part of a broader set of objectives of this investigation, which is supported by the National Science Foundation. While details of the micromechanical ULCF models are beyond the scope of this report, some basic background and application of the models is presented herein since they provide practical insights into the fracture behavior and an accurate means to extrapolate the limited brace test data.

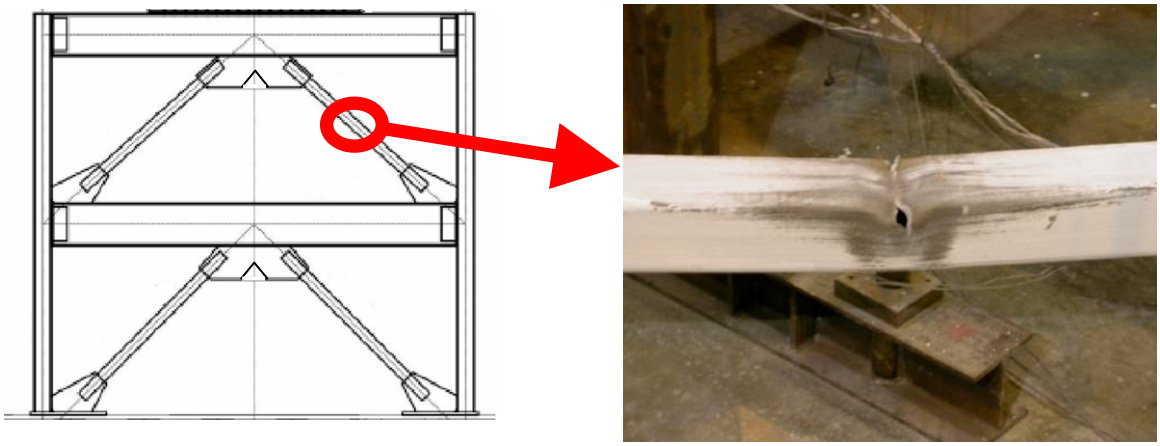

Figure 1.1: Experimental fracture at plastic hinge (Uriz and Mahin, 2004)

The organization of this report is as follows:

**Chapter 2** summarizes the experimental program, including the brace properties, experimental setup, applied loading histories, and test results. Design considerations and fabrication drawings are provided that show the dimensions and connection details for each specimen. The final section of the chapter presents a summary of the key experimental observations in terms of relevant performance limit states for each brace.

**Chapter 3** introduces the continuum-based Ultra Low Cycle Fatigue (ULCF) models to calculate the initiation of ductile fracture based on triaxial stress and strain data from finite element simulations of the braces. A brief discussion is presented to explain the importance of these fracture criteria to supplement the experimental program and provide valuable insights into brace performance.

**Chapter 4** presents design implications for SCBF systems based on the observations of this study. These include recommendations to improve the performance of SCBFs.

**Chapter 5** summarizes the significant findings and conclusions of the investigation.

**Appendix A** summarizes the measured material properties of the brace specimens, and **Appendix B** includes the hysteretic plots of each specimen along with parametric backbone curves to characterize the overall brace behavior for system analysis.

# 2. Summary of Experimental Program

## 2.1. Introduction

The overall objectives of the testing program are to examine earthquake-induced buckling and fracture behavior, considering both practical aspects of design and the validation of fracture simulation models. Details of the testing program were developed in consultation with the Structural Steel Educational Council and practicing engineers at Rutherford and Chekene (http://www.ruthchek.com/). The testing program consisted of nineteen large-scale tests of concentrically loaded HSS, pipe and W-sections. This chapter reviews the experimental setup, the design of the test specimens and loading protocols, and the performance variables investigated. Test results, including the buckling and fracture limit states and associated forces and deformations are summarized at the end of the chapter; and further details regarding the design implications are discussed in Chapters 4 and 5.

## 2.2. Experimental Setup

The tests were conducted at the UC Berkeley NEES facility located at the Richmond Field Station. The NEES facility offers state-of-the-art testing resources and versatility with respect to the application of boundary conditions, forces, and loading rates. More information on the NEES lab at Berkeley is available at: http://nees.berkeley.edu/.

As shown in Figures 2.1 and 2.2, the test setup consisted of the brace specimen installed in a test rig with two servo-hydraulic actuators, each of which has a force capacity of 220 kips and a stroke capacity of +/- 10 inches. The test rig provided a fixed-fixed boundary condition for the braces, where one brace connection was bolted directly to a large reaction block and the other end was attached to a moving cross-beam. The connection gusset plates were oriented so that braces buckled in the horizontal plane with an effective buckling length equal to the length of the brace. The entire setup was attached to the strong floor and stood approximately three feet high. The tests were performed in displacement control and the actuators were set in a master-slave feedback-control manner to minimize the in-plane rotation of the cross-beam and, thereby, maintained a fixed boundary condition at the translating end.

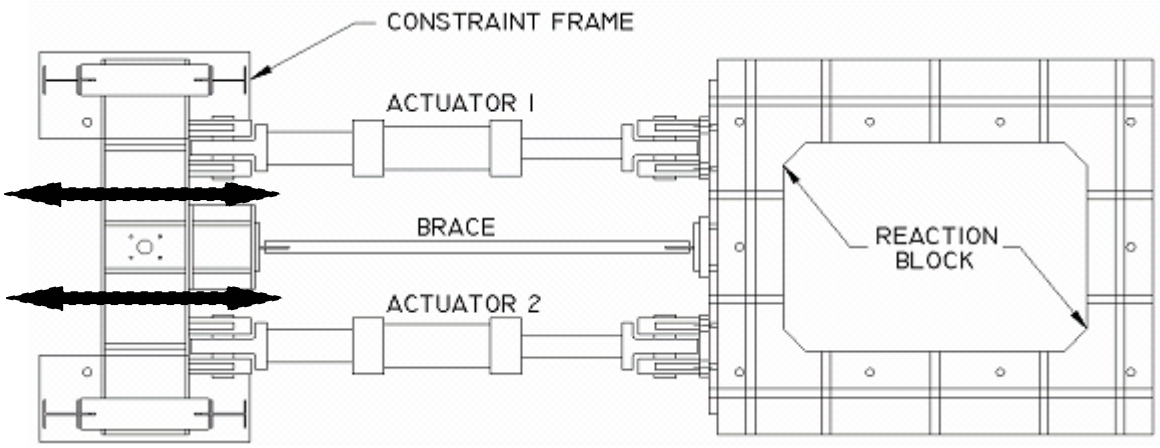


Figure 2.1: Plan view of the test setup at NEES Berkeley

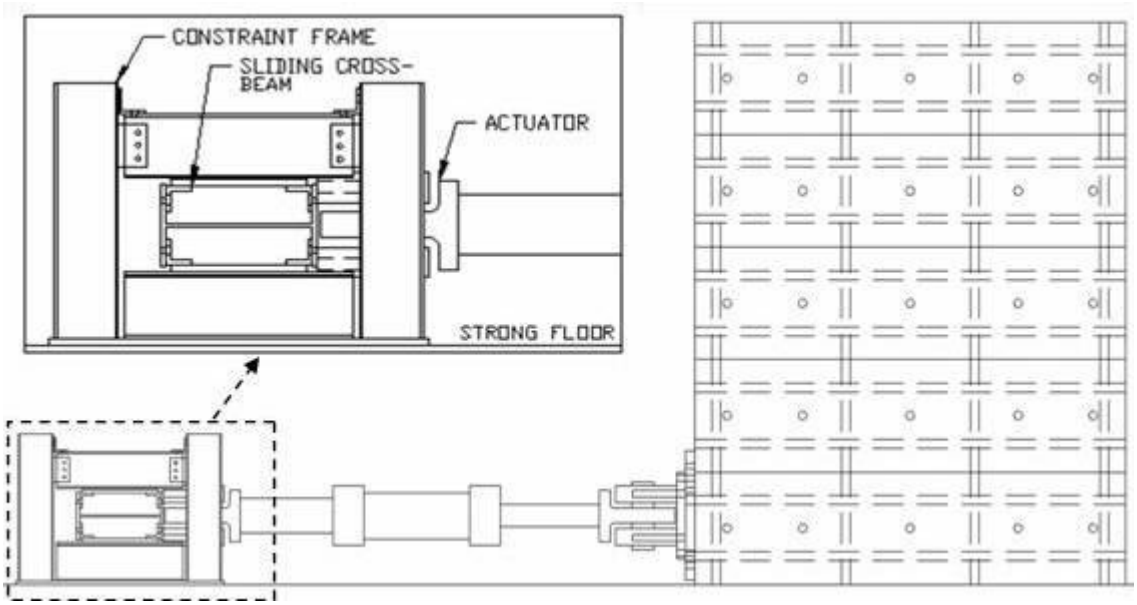


Figure 2.2: Elevation view of actuator, constraint frame and sliding cross-beam

## 2.3. Test Goals and Matrix

Shown in Table 2.1 is the testing matrix for the nineteen specimens, including information on the brace cross sections and loading variables. Eight of the specimens were square HSS, which are commonly used in SCBF design and known to be susceptible to fracture from previous studies (Uriz and Mahin, 2004). Pipe and wide-flange sections were selected for the other eleven tests since they were thought to perhaps provide improved fracture resistance. The slenderness ($KL_B/r$) and width-thickness (b/t or D/t) ratios were varied to examine their contribution to fracture behavior. For example, with comparable slenderness ratios, the two HSS sections provide a direct assessment of the influence of width-thickness ratios on brace performance. The alternative pipe sections and W12x16 allow for an assessment of slenderness effects combined with section properties. For the HSS and pipe sections, the width to thickness ratios are well within the AISC limits for SCBF braces, i.e., $b/t < 16.1$ for the grade 46 ksi HSS sections and $D/t < 36.5$ for the grade 35 ksi pipe sections. On the other hand, the flanges of the

 

grade 50 ksi W12x16 just exceed the AISC limit of $b/2t_f < 7.22$. Similarly, the slenderness of the HSS and pipe sections are within the limit of $KL_B/r < 4\sqrt{(E/F_y)}$ ($KL_B/r < 100$ for the HSS and $KL_B/r < 115$ for the pipe), whereas that of the W12x16 exceeds the limit ($KL_B/r < 96$).

Net-section reinforcement was examined in the pipe specimens, and the influence of concrete fill was examined in two of the HSS specimens. Loading variables include the loading cycle history (representing effects of far-field versus near-fault ground motions) and loading rates (quasi-static versus earthquake rate). A tension-dominated near fault loading history investigates net-section type fracture of end connections, especially for the pipe and wide flange braces. High loading rates, corresponding to those induced by an earthquake on a building with a 0.8 second period, were included to substantiate the use of quasi-static testing for characterizing seismic performance.

Table 2.1: Brace Specimens and Loading Variables

| Test # | Bracing Member | Loading History | Loading Rate | Width-thickness | $KL_B/r$ (K = 1.0) |
|---|---|---|---|---|---|
| 1 | HSS4x4x1/4 | Far-Field | Slow | 14.2 | 77 |
| 2 | HSS4x4x1/4 | Near-Fault (C) | Slow | 14.2 | 77 |
| 3 | HSS4x4x1/4 | Far-Field | Fast | 14.2 | 77 |
| 4 | HSS4x4x3/8 | Far-Field | Slow | 8.46 | 83 |
| 5 | HSS4x4x3/8 | Far-Field | Fast | 8.46 | 83 |
| 6 | Pipe3STD | Far-Field | Slow | 16.2 | 103 |
| 7 | Pipe3STD # | Far-Field | Slow | 16.2 | 103 |
| 8 | Pipe3STD # | Near-Fault (T) | First Pull Fast | 16.2 | 103 |
| 9 | Pipe3STD | Near-Fault (T) | First Pull Fast | 16.2 | 103 |
| 10 | Pipe5STD # | Near-Fault (T) | First Pull Fast | 21.6 | 64 |
| 11 | Pipe5STD | Near-Fault (T) | First Pull Fast | 21.6 | 64 |
| 12 | Pipe5STD # | Far-Field | Slow | 21.6 | 64 |
| 13 | Pipe5STD | Far-Field | Slow | 21.6 | 64 |
| 14 | W12x16 | Near-Fault (C) | Slow | 7.5* | 155* |
| 15 | W12x16 | Far-Field | Slow | 7.5* | 155* |
| 16 | W12x16 | Near-Fault (T) | Slow | 7.5* | 155* |
| 17 | HSS4x4x1/4 ** | Far-Field | Slow | 14.2 | 77 |
| 18 | HSS4x4x1/4 ** | Near-Fault (C) | Slow | 14.2 | 77 |
| 19 | HSS4x4x1/4 ## | Far-Field | Slow | 14.2 | 77 |

* exceed the limits of the AISC seismic provisions; # reinforcement not provided at the gusset plate net section; **concrete filled; ## reinforcement provided at mid-length; (C) asymmetric compression history; (T) asymmetric tension history

## 2.4. Description of Experimental Brace Specimens

Fabrication drawings of the brace specimens and connections are shown in Figures 2.3 through 2.6. The dimensions for the HSS and PipeSTD braces are listed in Table 2.2 and correspond to the labels shown in Figures 2.3 and 2.4. The W12x16 brace, whose details are quite different from the HSS and pipe, is shown separately in Figure 2.5. Table 2.3 summarizes the specified material properties for the braces, including the $R_y$ and $R_t$ factors (AISC, 2005) where $R_y$ is the ratio of expected yield strength to the minimum specified yield strength ($F_y$) and $R_t$ is the ratio of expected ultimate strength to the minimum specified ultimate strength ($F_u$).

 

Important features of the designs are summarized as follows –

- The specimens all have a total length of 10'-3" from end plate to end plate
- The provision of the "2t" fold line in the gusset plate was followed to allow for the development of a yield line during brace buckling (Astaneh, 1985 and 1998).
- Gusset plates were designed to prevent buckling (Astaneh, 1998)
- Gusset plates were designed to prevent yielding in tension (Whitmore, 1950).
- For all braces, except for specimens 7, 8, 10, and 12, net section reinforcement (Yang and Mahin, 2005) was provided to prevent net section fracture at slotted ends.
- Welds were detailed to avoid fracture
- End plates and bolts were designed considering prying action
- Design forces, determined by $R_y F_y A_g$, were used for all tension dominated actions

Note that the gusset plate slots in the brace specimens (Figure 2.4) are shorter than typical detailing practice where, for constructability, it is common to extend the slot approximately 1" beyond the gusset plate. Similarly, the net section reinforcing plates are slightly shorter than would typically be required to prevent net section fracture (refer Yang and Mahin, 2005). In addition, to ensure proper weld behavior, typical connection details do not allow the weld to continue to the end of the gusset plate as was permitted in these specimens.

Table 2.2: Design variables associated with Figure 2.3 and 2.4

| Cross section | QTY | BWL (in) | ET (in) | EW (in) | GW (in) | GL (in) | GWT (in) | RL (in) | RWT (in) | RW (in) | RT (in) |
|---|---|---|---|---|---|---|---|---|---|---|---|
| HSS4x4x1/4 | 6 | 10 | 2 | 10 | 6 | 11 ½ | 5/16 | 8 | ¼ | 2 | ¼ |
| HSS4x4x3/8 | 2 | 15 | 2 | 10 | 6 | 16 ½ | 7/16 | 8 | ¼ | 2 | 3/8 |
| Pipe3STD | 4* | 6 ½ | 1 ½ | 14 | 5 ½ | 8 | 5/16 | 6 | 3/16 | 2 | ¼ |
| Pipe5STD | 4* | 12 | 1 ½ | 14 | 7 ½ | 13 ½ | 3/8 | 11 | 3/16 | 3 | ¼ |

*Two braces were fabricated without reinforcing plates

Table 2.3: Nominal material properties as specified per ASTM and AISC

| Cross Section | Steel Type* | $A_g$ ($in^2$) | $F_y$* (ksi) | $F_u$* (ksi) | $R_y$ | $R_t$ |
|---|---|---|---|---|---|---|
| HSS4x4x1/4 | A500 Gr. B | 3.37 | 46 | 58 | 1.4 | 1.3 |
| HSS4x4x3/8 | A500 Gr. B | 4.78 | 46 | 58 | 1.4 | 1.3 |
| Pipe3STD (Type E) | A53 Gr. B | 2.23 | 35 | 60 | 1.6 | 1.2 |
| Pipe5STD (Type E) | A53 Gr. B | 4.30 | 35 | 60 | 1.6 | 1.2 |
| W12x16 | A992 | 4.71 | 50 | 65 | 1.1 | 1.1 |

* ASTM minimum values; $A_g$ as per AISC (2001)

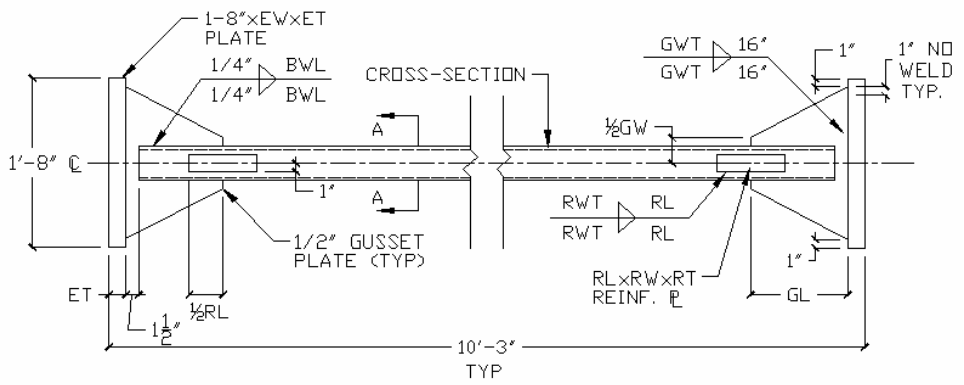


Figure 2.3: Fabrication drawing of HSS and PipeSTD braces

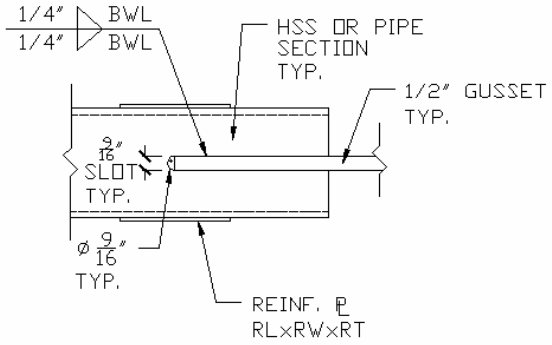


Figure 2.4: Typical connection detail for HSS and PipeSTD braces

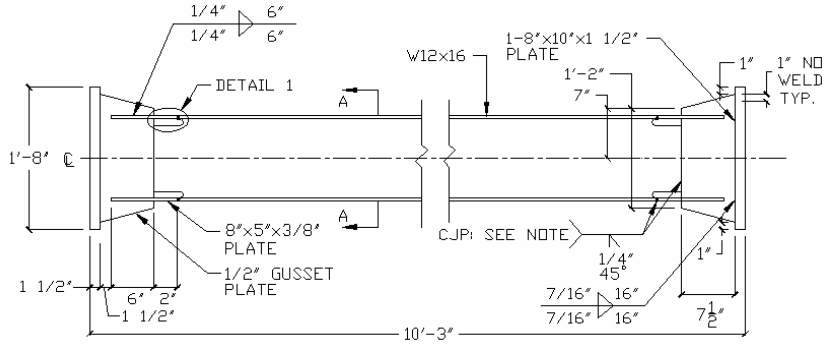


Figure 2.5: Fabrication drawing for W12x16 brace

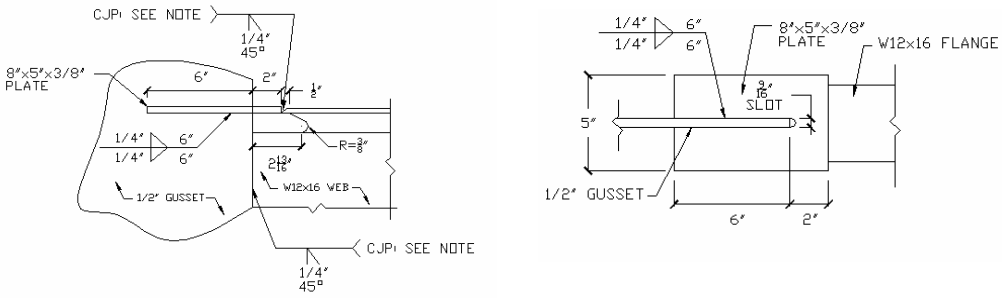


Figure 2.6: "Detail 1" in Figure 2.5

 

## 2.5. Description of Loading Histories Applied to Braces

The cyclic loading protocols for the brace tests were devised to impose deformation demands consistent with earthquake loading effects. Consequently, three important considerations controlled the design of the loading protocols: (1) Providing deformation demands – in terms of absolute deformation as well as numbers of cycles – consistent with real earthquakes; (2) Minimizing scale effects to allow for the generalization of the performance observations from the two-third scale tests to full-scale frames; and (3) Incorporating the effects of different types of ground motions, i.e. far-field versus near-fault conditions.

The loading protocols were developed considering the advantages and disadvantages of various published protocols, selecting a suitable one, and adapting it to the specific aims of this study. Sections 2.5.1, 2.5.1.1, and 2.5.2 describe the development of two such loading protocols. One loading history aims to represent the demands imposed by far-field (general, non-near fault) ground motions, while another aims to represent demands imposed by near-fault motions. It is important to note that in contrast to moment frame systems, where seismic drift demands are fairly stable (with respect to design variables – Gupta and Krawinkler, 1999), development of standardized loading protocols are more challenging for SCBFs since the deformation demands tend to be more sensitive to minor variations in subjective design decisions, owing to the wide variety of bracing configurations and the complex and irregular behavior of the bracing elements. For example, the slenderness ratio of the bracing elements can have a significant influence on drift ratios (Tremblay, 2000). In view of these issues, the loading protocols used for these studies intend to reflect the best estimates of seismic demands on SCBF systems based on analytical studies conducted by the authors and others.

### 2.5.1. Far-Field Loading Protocol

The far-field (or general) loading history was developed by adapting one from ATC-24 (ATC, 1992) to represent SCBF behavior. This protocol is based on nonlinear time history investigations by Krawinkler et al. (2000), who demonstrated that the dissipated energy demands that result from the testing protocol are consistent (under reasonable assumptions) with realistic seismic demands in ductile moment frames. The authors modified the moment frame loading protocol to braced frames using concepts outlined by Krawinkler et al. in its original development.

#### 2.5.1.1. Modification of SAC Far-Field Protocol

Figure 2.7 outlines the ATC/SAC loading protocol. The protocol is defined in terms of cycles of story drift angles of successively increasing magnitudes. As shown in the figure the loading history consists of three increasing sets of six cycles ($\theta = 0.00375$, $\theta = 0.005$, and $\theta = 0.0075$) followed by four cycles at the approximate yield drift of a moment frame ($\theta_Y = 0.01$), and four progressively increasing sets of two cycles each with the fourth set corresponding to the Maximum Considered Event – MCE level ($\theta = 0.015$, $\theta = 0.02$, $\theta = 0.03$, and $\theta_{MCE} = 0.04$).

 

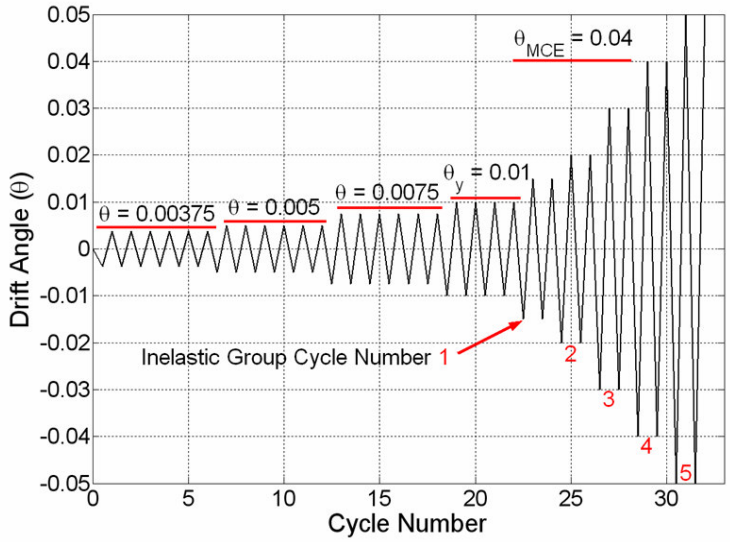


Figure 2.7: ATC/SAC protocol for moment frames

The modified ATC/SAC far-field protocol used in the current study for SCBF systems is illustrated in Figure 2.8 and Table 2.4. The four cycles at the MRF yield level (1% drift – load step 4; solid box in Table 2.4) are scaled to coincide with the onset of inelasticity in an SCBF system, typically the buckling displacement of the brace. Load steps 1-3 ($\theta = 0.00375$, $\theta = 0.005$, and $\theta = 0.0075$ from the original history) are scaled using the same factor. The intent of this modification is to ensure a relatively consistent number of inelastic damaging cycles between the SCBF and original ATC/SAC protocols. The justification for maintaining a similar number of inelastic cycles between the SCBF and MRF histories is based on the observations that (1) once a structure begins to yield, the period elongates so that the demands are more ground motion dependent rather than structure (initial stiffness) dependent and (2) recent research (Uriz and Mahin, 2004 and Tremblay, 2001) suggests that the MCE interstory drift level for SCBFs is in the 3-5% range, which is comparable to that for MRFs. Based on this reasoning, scale factors were developed that allowed the inelastic cycle set to increase such that (1) the number of inelastic cycles would be preserved between the ATC/SAC and the new protocol and (2) the largest cycles would reflect a drift level consistent with the $\theta_{MCE}$ ATC/SAC protocol. This entails some scaling of the intermediate cycles between the yield and MCE level (dashed box in Table 2.4). Refer Figure 2.8 and Table 2.4 for details.

 

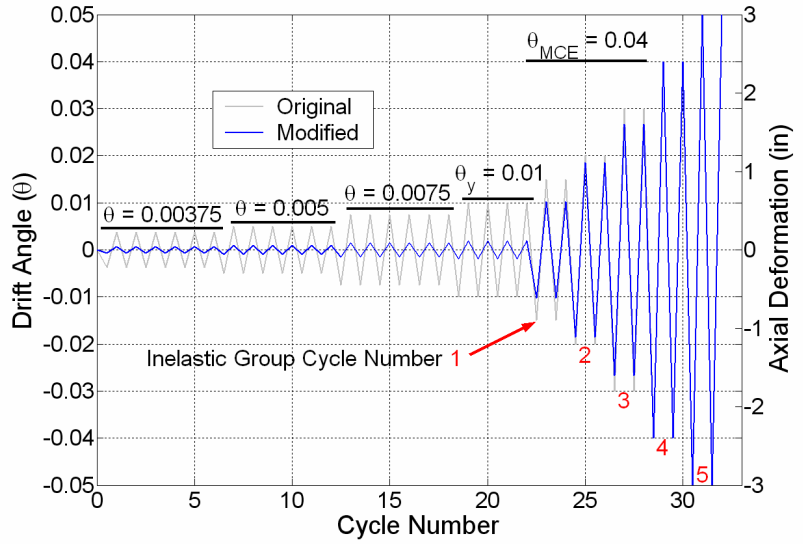


Figure 2.8: Modified SAC far-field loading protocol for SCBFs shown with original ATC/SAC protocol for MRFs

Table 2.4: Summary of loading protocol derivation

| | | Original SAC History | Modified SAC History | |
|---|---|---|---|---|
| Load Step | Number of Cycles | Peak θ (rads) | Peak $\Delta_a$ (in) | Peak θ (rads) |
| 1 | 6 | 0.00375 | 0.04 | 0.00075 |
| 2 | 6 | 0.005 | 0.06 | 0.001 |
| 3 | 6 | 0.0075 | 0.09 | 0.0015 |
| 4 | 4 | 0.01 | 0.12 | 0.002 |
| 5 | 2 | 0.015 | 0.61 | 0.01025 |
| 6 | 2 | 0.02 | 1.10 | 0.0185 |
| 7 | 2 | 0.03 | 1.59 | 0.02675 |
| 8 | 2 | 0.04 | 2.38 | 0.04 |
| 9 | 2 | 0.05 | 2.99 | 0.05 |

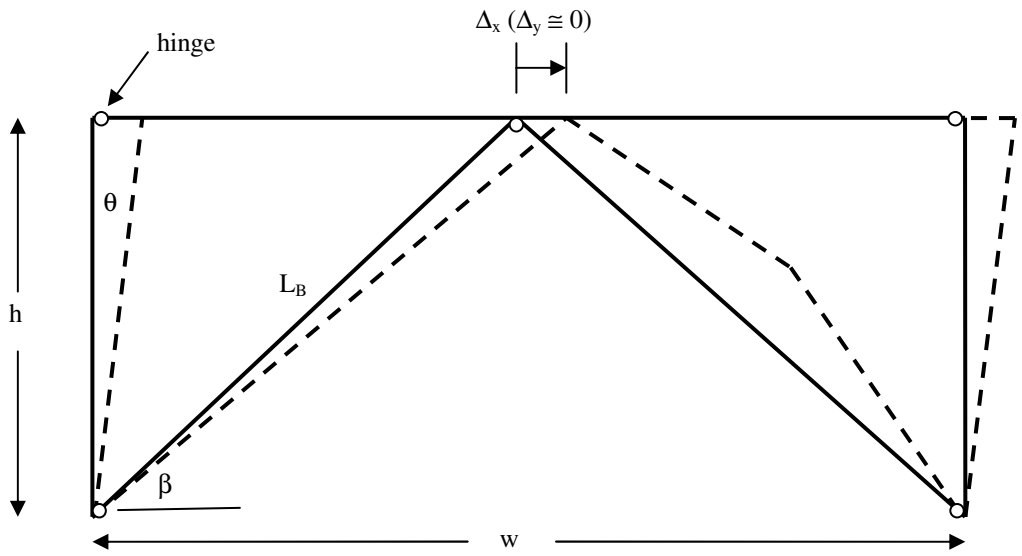


Figure 2.9: Schematic of a typical story within a Chevron frame

The brace deformations are related to the interstory drift angle using a simple kinematic relationship as shown in Figure 2.9. Referring to this idealized figure, the axial deformation of a brace ($\Delta_a$) is described in terms of the original length ($L_B$) and orientation ($\beta$) of the bracing member, and the story drift of the frame ($\theta$) by the following equation:

$$\Delta_a = L_B\sqrt{1+2\theta\cos\beta\sin\beta+\theta^2\sin^2\beta} - L_B \qquad (2.5.1)$$

This relationship between the drift angle, as prescribed in the loading protocol, and brace deformations assumes no significant flexural effects in the beam or columns. For the Chevron bracing configuration, this assumption implies that Eq. 2.5.1 will slightly overestimate the brace deformations, for a given drift angle, since the beam flexure will add flexibility to the system.

Assuming that the brace is oriented at $\beta = 45°$ and an undeformed brace length of $L_B$ = 118" (the specimen length of 10'-3" minus the 4" end plate and 1.5" fold line dimensions), the axial deformation history for the brace can be related to the story drift loading history. For example, this geometry implies an axial brace deformation of 0.59 inches for a story drift angle of 0.01 radians (1% drift), i.e.,

$$\Delta_a = 118\sqrt{1+2(0.01)\cos 45^\circ \sin 45^\circ + (0.01)^2 \sin^2 45^\circ} - 118 = 0.59$$

$$\Delta_a \approx 59\theta$$

Using this relationship, the axial brace loading history is shown in Table 2.4 alongside the corresponding drift based history. In the cyclic history, positive drift angles or axial displacements are assumed to correspond to tensile brace loading and negative displacements to compressive loading.

 

A brief validation exercise was carried out to examine if the demands produced by the protocol were realistic and consistent with the intent of the ATC/SAC protocol. For this purpose, a methodology similar to the one used by Krawinkler et al. (2000) was applied. The central idea of this is to determine if, for any absolute level of deformation, the cumulative plastic deformation is consistent with that expected in an earthquake. Assuming cumulative plastic rotation to be indicative of damage, the protocol enables the transfer of results from the experiments to performance assessment of systems at similar absolute levels of deformations during earthquakes. Since analytical results of damage accumulation in SCBF systems were not available, the validation relies on a comparison of the cyclic damage accumulation for braces using the modified protocol to the implied damage for moment frame connections using the SAC protocol. Using this approach, the cumulative plastic deformations (indicative of damage) are compared to the inelastic cyclic group number in Figure 2.10. These data show good overall agreement in the accumulation of inelastic damage for the five brace specimen types (differentiated by their buckling displacement) and the corresponding curve for the ATC/SAC protocol.

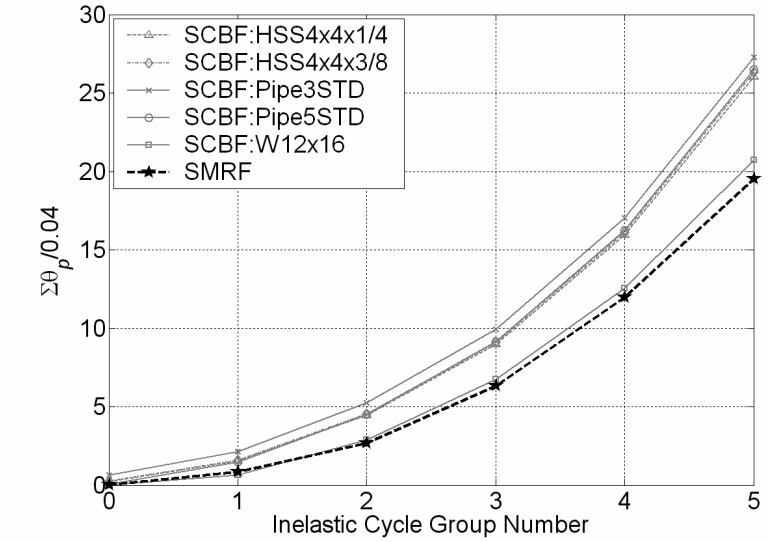


Figure 2.10: Comparison of modified protocol for SCBFs and the original protocol for a SMRF

### 2.5.2. Description of Near-Fault Loading Histories

To reflect demands imposed by near-fault ground motions, two loading protocols – asymmetric compression and asymmetric tension – were used for several of the brace tests. As with the general protocol (described previously) the near-field protocol is based on a similar one developed in the SAC project for moment frames. These loading protocols are illustrated in Figures 2.11 and 2.12.

As shown in Figure 2.11, the compression dominated history is identical to the ATC/SAC near-fault protocol. However, following completion of the near-field protocol, the far-field loading protocol (of Figure 2.8) is appended so as to extract additional information from the test in the event that the brace survives the near-fault loading. Aside from providing data for

validating the ductile fracture models, this subsequent loading is envisioned to represent an aftershock earthquake that follows the first large pulse of the main earthquake fault rupture.

The tension dominated history (Figure 2.12) consists of a large monotonic pull followed by subsequent cycles. This protocol was designed as a worst-case scenario for tension-sensitive details such as unreinforced net-section connections at slotted ends of the brace. A similar approach was adopted by Yang and Mahin (2005). The tension history is similar to the near fault compression history, except that to ensure that the brace would not buckle before the main tension pull, the tension history does not include any large compression cycles before the first tension pull. Additionally, to ensure significant inelastic tension response during its initial loading excursion, the amplitude of the initial tension pull is 8% drift, which is larger than the 6% drift used in the compression history.

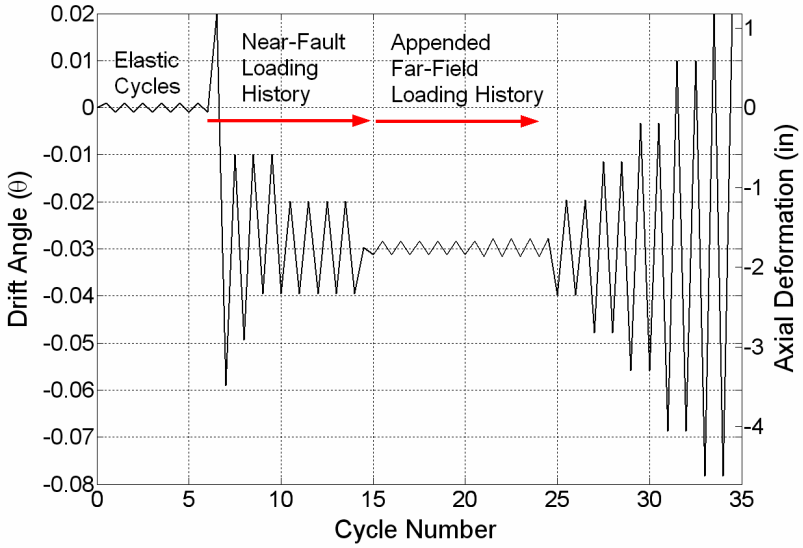


Figure 2.11: Asymmetric compression near-fault history

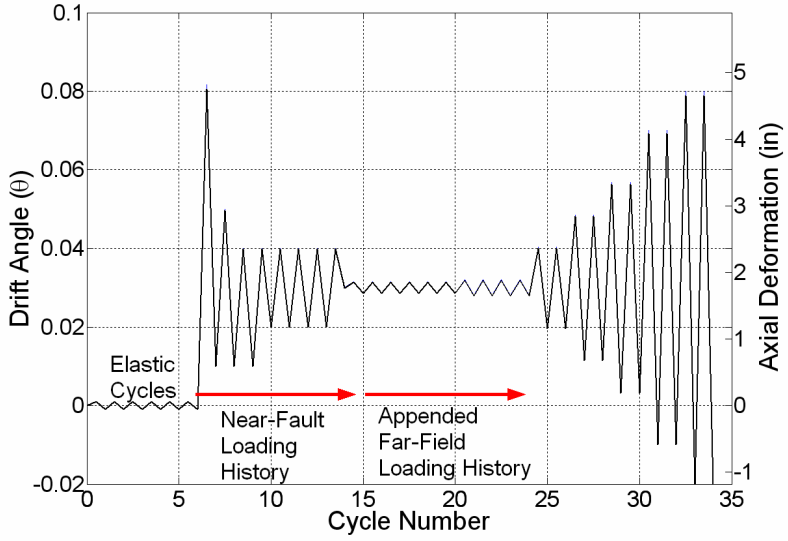


Figure 2.12: Asymmetric tension near-fault history

## 2.6. Summary of Experimental Results

This section summarizes results from the nineteen brace tests. For each test, key limit states are monitored, among the two most significant being the onset of local buckling and the initiation of fracture. Other relevant data reported include the critical buckling load, maximum tensile load, and initial stiffness. This section summarizes the key data and observations, while the detailed hysteretic load-deformation plots for all experiments are provided in Appendix B. Results of two tests (#1 and #2), which are generally representative of the brace behavior, are discussed in detail in section 2.6.3; and, detailed discussion on tension dominated loading is presented in section 2.6.4. Further discussion of the design implications of the test results is presented in section 4.

### 2.6.1. Qualitative Description of Experimental Limit States

All experiments subjected to cyclic loading qualitatively follow a similar sequence of events leading up to failure of the brace. The initial elastic cycles do not induce any visually observable deformation in the brace. The first major limit state is brace buckling, which is evident by large lateral deformations and accompanied by flaking of the whitewash paint due to large strains associated with kinking at the end gusset plates and at mid-length of the brace. As shown in Figure 2.13, localized yielding in the gusset plates and mid-point hinge becomes more severe as the amplitude of loading increases. Subsequently, a local buckle typically forms at the middle hinge, which triggers ductile fracture soon thereafter. The photos of Figure 2.14 are fairly representative of the local buckling and fracture observed in most tests. Upon further cycling, the rupture propagates in a ductile manner across the section, i.e., for square HSS, the buckled face ruptures first followed by the sides. Finally, at some point during a subsequent tensile excursion, the entire cross section fractures suddenly, severing the brace.

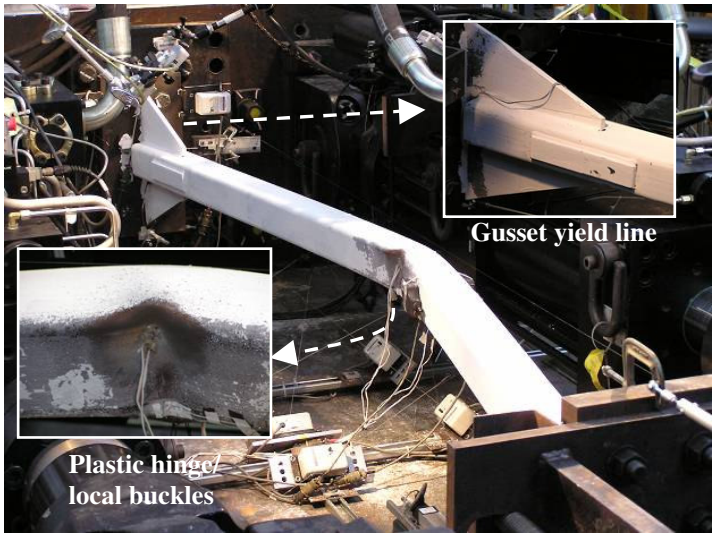

Figure 2.13: Global buckling, local buckling, and gusset yield line

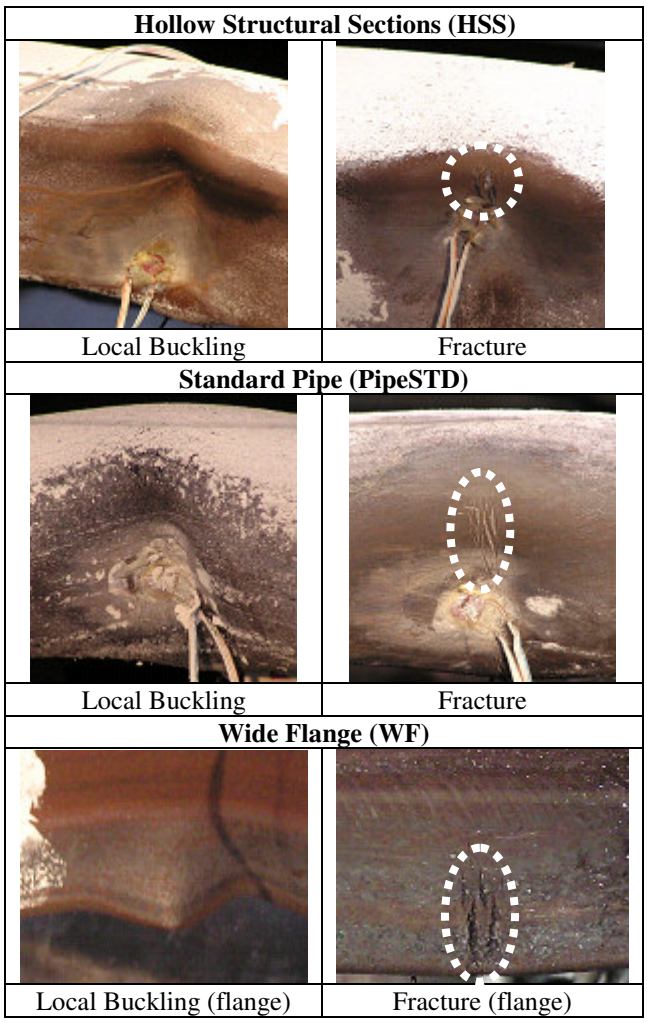


Figure 2.14: Typical local buckling and fracture initiation limit states of the experimental cross sections

### 2.6.2. Summary of brace performance for all tests

Table 2.5 summarizes the measured stiffness and peak resistance of each brace specimen, including comparisons to calculated values based on the AISC design requirements. Table 2.6 summarizes data describing deformation indices corresponding to the four limit states of global buckling, local buckling, fracture initiation, and strength loss of the member. Results in these two tables provide a means to compare and contrast the influence of various design parameters and are referenced in discussions later in the report. The drift indices reported in Table 2.6 for global buckling correspond to the point at which the critical compressive load is reached, whereas data for the other limit states are presented in terms of the maximum drifts sustained by the member before the limit state event was observed. For example, the drift corresponding to fracture initiation is the maximum drift sustained prior to this event, which could be larger than the drift at which the fracture occurred during reverse cyclic loading. This permits the use of the simple drift index to track these results, as opposed to a more complex damage index that employs some type of cyclic counting scheme, which would be somewhat subjective and less intuitive than the

simple drift index. More complete data on the exact instants of the limit state events for each test are summarized in Appendix B.

Referring to Table 2.5, in general the measured initial elastic stiffness was within 7% of the calculated value of $EA/L_B$, where the differences are primarily due to resolution of the measurements and non-ideal end connections. The measured tensile resistances at 2% story drift (corresponding to design level drift) were about 11% larger than the expected yield strength, where the latter is calculated using nominal values for $R_yF_yA_g$. The measured maximum tensile strengths were about 15% larger than the expected yield strengths and about 6 to 8% less than the expected ultimate strengths ($R_tF_uA_g$). Thus, while the expected yield and ultimate strengths bracket the measured peak strength, the tensile resistance exceeds the expected yield strength over most of the inelastic loading histories. In the most extreme case, the measured peak response was 25% larger than the expected yield strength (Test #15). Test #8 and 10 were not reinforced at the net section and, consequently, failed at the net section during a tension dominated near-field loading history. The measured compressive strengths ranged from about 1.0 to 1.7 times the expected compressive strengths, where the latter are calculated using nominal expected values of $R_yF_y$ in the AISC column curve.

Referring to Table 2.6, the drifts corresponding to brace lateral buckling (global buckling) ranged from 0.2% to 0.35% for the tests with cyclic far-field loading. While member slenderness and concrete fill (Test #17) had some influence on the buckling drifts, the differences observed in Table 2.6 are not significant. For the compression dominated near-field loading (Tests #2, 14, and 18), the buckling drifts increased to about 1% to 1.3%, indicating the extent of cyclic loading effects on the buckling drift. The buckling drifts for tests (#9 – 11 and 16) with tension dominated near-field loading are listed in Table 2.6 for completeness but otherwise are difficult to interpret. There were larger differences between tests for the onset of local buckling, which indicates the sensitivity of the local buckling limit state to cross sectional shape and width-thickness ratios. For the cyclic far-field loading, the drifts at local buckling ranged from 1.9% to 5%, where the larger resistance occurred in the more stocky HSS sections and the pipe and W-section. Comparing Tests #1 and 17, while the concrete fill postponed local buckling in the HSS sections, the difference was not as significant as for some of the other parameters. Tests #1 and 19 showed the lowest drift level sustained prior to local buckling (1.85%) due in part to the large width-thickness ratio and the unsymmetrical buckling observed in Test #19 (more details on these aspects are discussed in chapter 4). As observed with overall buckling, the onset of local buckling occurred at larger drifts in the specimens subjected to compression dominated near-fault loading. In general, fracture initiation and strength loss closely followed the local buckling, and the trends with regard to drift endurance values are similar for these except that the differences between far-field and near-fault loadings were not as significant as with global or local buckling. For the far-field and compression dominated near-fault loadings, fracture initiation and loss of strength occurred at about 2 to 8% drift angles. Tests with the tension-dominated near fault loading generally had larger fracture endurance, largely because the local buckling was delayed by the tension loading.

 

### 2.6.3. Observations of Typical Brace Buckling Behavior

Referring to Table 2.1, Test #1 featured an HSS4x4x1/4 subjected to the far-field loading history shown in Figure 2.15a. Figure 2.15b shows the corresponding hysteretic load-deformation plot of this test. The key limit states of global buckling, local buckling, fracture initiation and loss of tensile strength due to fracture are indicated on both figures. Figure 2.15a shows both the axial deformation of the brace and the corresponding drift (related by Equation 2.5.1) to facilitate a more appropriate correlation of each limit state to a system performance level.

Global buckling is defined as the first point during a compressive excursion that the peak compressive load of the brace is reached. Local buckling is defined more subjectively as a visible distortion in the cross sectional shape. Referring to Figure 2.15a, for Test #1, local buckling was observed at cycles corresponding to a story drift level of 1.85%. Fracture initiation is documented in a similar manner to local buckling by visually observing metal rupture on the surface in the region of the plastic hinge. For Test #1, initial ductile crack initiation (fracture) occurred at a drift of 1.7% during a cycle set with a maximum amplitude of 2.7%. Strength loss in tension is marked by a sudden drop in load due to fracture and significant loss of cross sectional area. This is the most apparent limit state indicated on the hysteretic plot in Figure 2.15b. For Test #1, strength loss occurred during the same set of cycles (amplitude of 2.7%) as the initial fracture, at a drift of 2.5%. This type of information is summarized for all the experiments in Table 2.6, which is referred to in subsequent sections (especially in Chapter 4).

Other relevant properties, such as initial stiffness, buckling displacement, and strength in tension and compression, are summarized in Table 2.5. For Test #1, the values are labeled on the force deformation plot of Figure 2.15b. The AISC (2005) values for strength, along with analytical values for stiffness and displacements are included in Table 2.5. For example, Test #1 had a measured maximum tensile resistance of 247 kips and measured compressive resistance of 157 kips, whereas the corresponding values calculated as per AISC are:

$$R_y F_y A_g = 1.4(46\,\text{ksi})(3.37\,\text{in}^2) = 217\,\text{kips}$$

$$R_t F_u A_g = 1.3(58\,\text{ksi})(3.37\,\text{in}^2) = 254\,\text{kips}$$

$$P_n = F_{cr} A_g = (30.8\ \text{ksi})(3.37\ \text{in}^2) = 104\,\text{kips}$$

$$\lambda = \frac{KL_B}{\pi r}\sqrt{\frac{F_y}{E}} = \frac{1.0(118")}{\pi(1.52")}\sqrt{\frac{46\ \text{ksi}}{29{,}000\ \text{ksi}}} = 0.98\ \text{(inelastic)}$$

$$F_{cr} = F_y 0.658^{\lambda^2} = 30.8\,\text{ksi}$$

The estimated critical buckling loads presented in Table 2.5 use $R_y$ to account for the increase in yield stress from the minimum specified value to the expected value:

$$P_{cr,\,exp} = F_{cr\text{-}R_y} A_g = (36.5\ \text{ksi})(3.37\ \text{in}^2) = 123\,\text{kips}$$

$$\lambda = \frac{KL_B}{\pi r}\sqrt{\frac{R_y F_y}{E}} = \frac{1.0(118")}{\pi(1.52")}\sqrt{\frac{1.4(46\ \text{ksi})}{29{,}000\ \text{ksi}}} = 1.16\ \text{(inelastic)}$$

$$F_{cr\text{-}R_y} = R_y F_y 0.658^{\lambda^2} = 36.5\,\text{ksi}$$

Figure 2.16a and 2.16b depict the equivalent response and limit states of an HSS4x4x1/4 specimen subjected to a near-fault compression dominated loading history (Test #2). The figures show that local buckling occurred during the first large compressive pulse of the cyclic history (at a drift of 2.5%). However, the brace cycled at a residual drift of 3% for the remainder of the test, and as a result, delayed fracture because tensile strains were kept small at this residual compressive drift level. Figure 2.16b also shows that the compressive buckling load decreased substantially (157 to 119 kips) compared to Test #1 due to considerable brace elongation and yielding during the first pull to 2%.

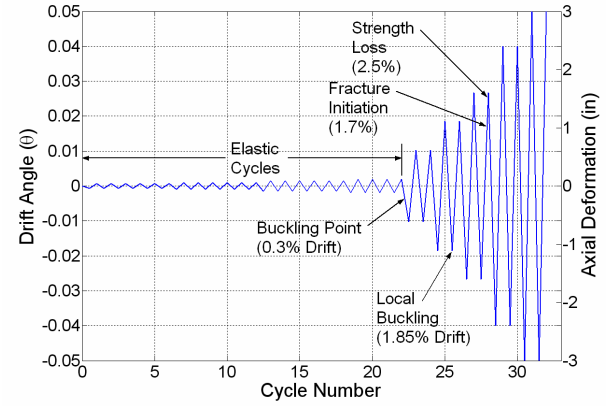


Figure 2.15a: Displacement history for Test #1

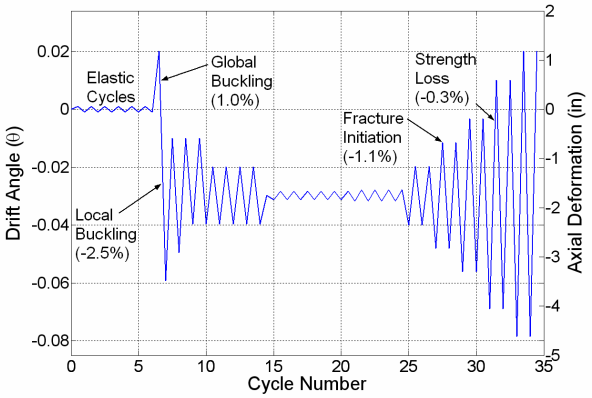


Figure 2.16a: Displacement history for Test #2

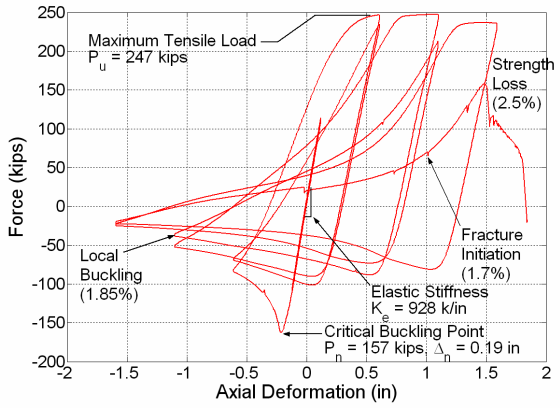


Figure 2.15b: Force vs. displacement history for Test #1

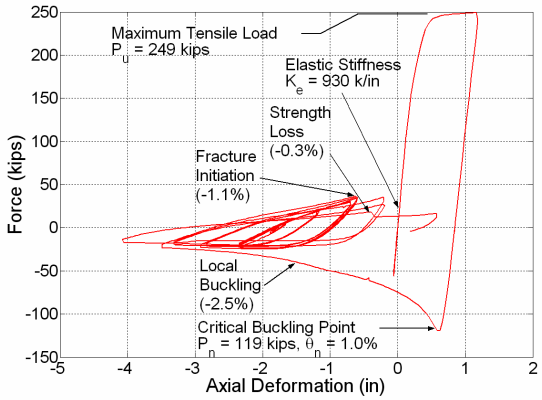


Figure 2.16b: Force vs. displacement history for Test #2

 

### 2.6.3. Observation of Typical Net-Section Tension Fracture

Tension dominated near-fault tests of the PipeSTD and wide-flange sections (Tests #8 – 11 and 16) provide data on the fracture performance of the net section at the connection. This is in contrast to the other specimens, such as the HSS sections with net section reinforcement or the compression dominated pipe and wide-flange tests, where fracture at the net section was not a critical limit state. The unreinforced net sections of the PipeSTD and wide-flange connections proved to be quite ductile and failed at drifts that exceeded the anticipated performance. For example, the Pipe3STD and Pipe5STD bracing members with unreinforced net sections fractured at drifts of 5.0% and 6.4%, respectively. The PipeSTD members with reinforced net sections and the W12x16 specimen sustained monotonic tensile drifts of 8.0% without fracturing.

The large deformations observed in Tests #8 – 11 and 16 are reassuring, given that the maximum measured tensile strengths were significantly larger than the expected yield strengths ($R_yF_yA_g$) of the braces. For example, the ratio of measured maximum forces to the calculated expected yield strengths are as high as 1.25 in Test #16 (W12x16 subjected to a tension near-fault history) and 1.21 in Test #12 (Pipe5STD during tension near-fault) and #18 (concrete-filled HSS4x4x1/4 during far-field loading). However, from a connection design perspective, this high ratio might produce large tensile demands in the connections. In this context, it is important to note that while the maximum tensile force, measured at drifts as large as 4-5%, may exceed the expected seismic demands for SCBFs, it may be more appropriate to compare the expected yield strength to the measured forces at drifts of 2%, which has previously been suggested as a more appropriate design basis for SCBF systems (Uriz and Mahin, 2004). The ratios of the measured strengths at 2% drift to the expected yield strengths are 1.09 and 1.16 for Tests #12 and #16, respectively. Note that with the exception of Test #18, the maximum measured strengths are all less than the calculated expected ultimate strengths ($R_tF_uA_g$). The design implications of these data are discussed further in section 4.4.

 

Table 2.5: Measured and Calculated Stiffness, Resistance, and Displacement

| Test # | Bracing Member | Stiffness | | | Tensile Resistance | | | | | | | Compressive Resistance | | | Buckling Displacement | |
|---|---|---|---|---|---|---|---|---|---|---|---|---|---|---|---|---|
| | | Meas. | Calc. | Ratio | Meas. | Meas. | Calc. | Calc. | Ratio | Ratio | Ratio | Meas. | Calc. | Ratio | Meas. | Calc. |
| | | $K_{e(m)}$ (k/in) | $K_{e(c)}$ (k/in) | $\frac{K_{e(m)}}{K_{e(c)}}$ | $P_{max}$ (k) | $P_{2\%}$ (k) | $P_{y,exp}$ (k) | $P_{u,exp}$ (k) | $\frac{P_{max}}{P_{y,exp}}$ | $\frac{P_{2\%}}{P_{y,exp}}$ | $\frac{P_{max}}{P_{u,exp}}$ | $P_{c,max}$ (k) | $P_{cr,exp}$ (k) | $\frac{P_{c,max}}{P_{cr,exp}}$ | $\theta_{c,max}$ (%) | $\frac{P_{cr,exp}}{0.59K_{e(c)}}$ |
| 1 | HSS4x4x1/4 | 928 | 832 | 1.12 | 247 | 247 | 217 | 254 | 1.14 | 1.14 | 0.97 | 157 | 123 | 1.28 | -0.3 | -0.25 |
| 2 | HSS4x4x1/4 | 930 | 832 | 1.12 | 249 | 249 | 217 | 254 | 1.15 | 1.15 | 0.98 | 119 | 123 | 0.97 | 1.0 | -0.25 |
| 3 | HSS4x4x1/4 | 910 | 832 | 1.09 | 255 | 255 | 217 | 254 | 1.18 | 1.18 | 1.00 | 161 | 123 | 1.31 | -0.34 | -0.25 |
| 4 | HSS4x4x3/8 | 1236 | 1180 | 1.05 | 348 | 348 | 308 | 360 | 1.13 | 1.13 | 0.97 | 186 | 159 | 1.17 | -0.29 | -0.23 |
| 5 | HSS4x4x3/8 | 1051 | 1180 | 0.89 | 362 | 362 | 308 | 360 | 1.18 | 1.18 | 1.01 | 184 | 159 | 1.16 | -0.33 | -0.23 |
| 6 | Pipe3STD | 583 | 546 | 1.07 | 132 | 129 | 125 | 161 | 1.06 | 1.03 | 0.82 | 80 | 54 | 1.50 | -0.27 | -0.17 |
| 7 | Pipe3STD# | 575 | 546 | 1.05 | 130 | 128 | 125 | 161 | 1.04 | 1.02 | 0.81 | 84 | 54 | 1.57 | -0.27 | -0.17 |
| 8 | Pipe3STD#* | 603 | 546 | 1.10 | 144 | 135 | 125 | 161 | **1.15** | **1.08** | 0.89 | N/A | N/A | N/A | N/A | N/A |
| 9 | Pipe3STD | 601 | 546 | 1.10 | 149 | 136 | 125 | 161 | **1.19** | **1.09** | 0.93 | 57 | 54 | 1.16 | 7.0 | -0.17 |
| 10 | Pipe5STD#* | 1124 | 1052 | 1.07 | 279 | 254 | 241 | 310 | **1.16** | **1.05** | 0.90 | N/A | N/A | N/A | N/A | N/A |
| 11 | Pipe5STD | 1162 | 1052 | 1.10 | 292 | 262 | 241 | 310 | **1.21** | **1.09** | 0.94 | 127 | 174 | 0.73 | 6.8 | -0.28 |
| 12 | Pipe5STD# | 1083 | 1052 | 1.03 | 243 | 237 | 241 | 310 | 1.01 | 0.98 | 0.78 | 177 | 174 | 1.01 | -0.3 | -0.28 |
| 13 | Pipe5STD | 1107 | 1052 | 1.05 | 241 | 241 | 241 | 310 | 1.00 | 1.00 | 0.78 | 181 | 174 | 1.04 | -0.3 | -0.28 |
| 14 | W12x16 | 1223 | 1153 | 1.06 | 287 | 287 | 259 | 337 | 1.11 | 1.11 | 0.85 | 92 | 56 | 1.65 | 1.3 | -0.08 |
| 15 | W12x16 | 1136 | 1153 | 0.99 | 286 | 286 | 259 | 337 | 1.10 | 1.10 | 0.85 | 93 | 56 | 1.67 | -0.16 | -0.08 |
| 16 | W12x16 | 1184 | 1153 | 1.03 | 323 | 300 | 259 | 337 | **1.25** | **1.16** | 0.96 | 75 | 56 | 1.34 | 7.2 | -0.08 |
| 17 | HSS4x4x1/4** | 941 | 832 | 1.13 | 257 | 257 | 217 | 254 | 1.18 | 1.18 | 1.01 | 194 | 123 | 1.58 | -0.36 | -0.25 |
| 18 | HSS4x4x1/4** | 949 | 832 | 1.14 | 263 | 263 | 217 | 254 | 1.21 | 1.21 | 1.04 | 136 | 123 | 1.11 | 0.9 | -0.25 |
| 19 | HSS4x4x1/4## | 937 | 832 | 1.13 | 249 | 249 | 217 | 254 | 1.15 | 1.15 | 0.98 | 163 | 123 | 1.33 | -0.35 | -0.25 |
| | | | Mean | 1.07 | | | | Mean | 1.14 | 1.11 | 0.92 | | Mean | 1.27 | | |
| | | | Median | 1.07 | | | | Median | 1.15 | 1.11 | 0.94 | | Median | 1.28 | | |
| | | | σ | 0.06 | | | | σ | 0.07 | 0.07 | 0.08 | | σ | 0.26 | | |

*failure at net section (otherwise at midpoint); #reinforcement not provided at the net section; **concrete filled; ##reinforcement at midpoint

Table 2.6: Experimental limit states – defined per maximum drift – see Appendix B for exact locations

| | | | Global Buckling | Local Buckling | Fracture Initiation | Strength Loss |
|---|---|---|---|---|---|---|
| **Test #** | **Bracing Member** | **Loading History** | **Drift (%)** | **Drift (%)** | **Drift (%)** | **Drift (%)** |
| 1 | HSS4x4x1/4 | FF | 0.3 | 1.85[(ex)] | 2.68[(ex)] | 2.68[(ex)] |
| 2 | HSS4x4x1/4 | NF (C) | 1.0 | 2.5 | 6.0 | 6.0 |
| 3 | HSS4x4x1/4 | FF (EQ) | 0.34 | 2.1 | 2.1 | 2.1 |
| 4 | HSS4x4x3/8 | FF | 0.29 | 5.0 | 5.0 | 5.0 |
| 5 | HSS4x4x3/8 | FF (EQ) | 0.33 | 4.3 | 4.3 | 4.3 |
| 6 | Pipe3STD | FF | 0.27 | 5.0 | 5.0 | 5.0 |
| 7 | Pipe3STD# | FF | 0.27 | 5.0 | 5.0 | 5.0 |
| 8 | Pipe3STD#* | NF (T, EQ1) | N/A | N/A | 5.0 (Monotonic) | 5.0 (Monotonic) |
| 9 | Pipe3STD | NF (T, EQ1) | 7.0 | 8.0 | 8.0 | 8.0 |
| 10 | Pipe5STD#* | NF (T, EQ1) | N/A | N/A | 6.4 (Monotonic) | 6.4 (Monotonic) |
| 11 | Pipe5STD | NF (T. EQ1) | 6.8 | 8.0 | 8.0 | 8.0 |
| 12 | Pipe5STD# | FF | 0.3 | 2.68 | 2.68 | 4.0 |
| 13 | Pipe5STD | FF | 0.3 | 2.68 | 2.68 | 2.68 |
| 14 | W12x16 | NF (C) | 1.3 | 6.0 | 6.0 | 6.0 |
| 15 | W12x16 | FF | 0.16 | 5.0 | 5.0 | N/A |
| 16 | W12x16 | NF (T) | 7.2 | 8.0 | 8.0 | 8.0 |
| 17 | HSS4x4x1/4** | FF | 0.36 | 2.68 | 2.68 | 3.6 |
| 18 | HSS4x4x1/4** | NF (C) | 0.9 | 7.9 | 7.9 | 7.9 |
| 19 | HSS4x4x1/4## | FF | 0.35 | 1.85 | 1.85 | 1.85 |

*failure at net section (otherwise at midpoint); #reinforcement not provided at the net section; **concrete filled; ##reinforcement at midpoint, EQ - entire test was performed at an EQ rate; EQ1 - only first large pull was performed at an EQ rate; FF - Far-Field; NF -Near-Fault;

**(ex):** The figure below shows the actual locations of the limit states for Test #1 (identical to Figure 2.15a). However, the above table reports the maximum sustained drift before each event (except for global buckling). For example, the largest drift that the brace experienced without local buckling (LB) was the first push to 1.85%; similarly the largest tensile drift sustained prior to fracture initiation (FI) was the first pull to 2.68% and since strength loss (SL) occurred on the same ramp, an equivalent maximum drift is reported. The exact instants when these limit states occurred can be found in Appendix B.

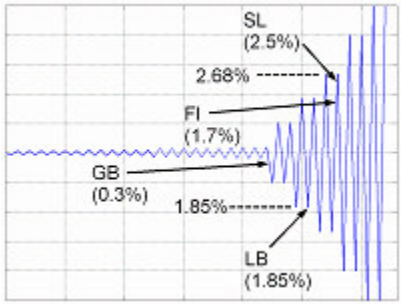

# 3. Introduction to continuum-based fracture and fatigue predictive models

This section provides a brief overview of the micromechanics-based models for fracture and fatigue that the brace tests aim to validate. The approach relies upon continuum finite element analyses to characterize the localized stress and strain states due to global and local buckling. These stress and strain data are input to the proposed fracture model, which accounts for the effect of triaxial stress on plastic strain capacity and the cyclic accumulation of damage. In this chapter, the motivation for developing micromechanics-based fracture models is introduced, followed by an example to illustrate their application and accuracy, relative to the brace test data. Finally, instances are examined where the models can be used to develop insights into localized effects that cause fracture (Figure 3.1) and extend the results of the nineteen brace tests presented in this study. The fracture simulation models provide a powerful tool for conducting parametric studies through a wide range of brace properties that affect ductility and fracture performance. These parametric studies can be used to identify more comprehensive trends and generate guidelines for the design and detailing of SCBFs and other systems.

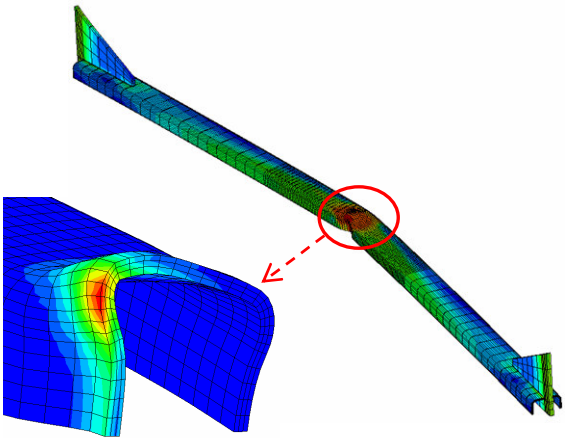

Figure 3.1: Buckled Shape of HSS brace

## 3.1. The Need for Fundamental Physics-Based Models to Predict Fracture and Fatigue in Steel

Prevailing approaches to characterize fracture/fatigue performance of braced frame and other structural components are based mostly on empirical or semi-empirical methods. For braces, previous research has relied on critical longitudinal strain measures, or cycle counting and fatigue-life approaches (Tang and Goel, 1989). Recent studies (Uriz and Mahin, 2004) have applied similar techniques through fiber-based elements to simulate localized fracture strain demands at a fiber within a cross section. While these approaches represent important advances in the fatigue-fracture prediction methodology for structures, they do not directly incorporate the effects of local buckling or the complex interactions of stress and strain histories that trigger crack initiation in these components. Consequently, large-scale testing is still required to characterize the fracture performance of these details (Herman et al., 2006).

In part, the dependence on simplistic or semi-empirical, experiment-based approaches can be attributed to the lack of computational resources required to simulate phenomena such as local buckling that create localized stress and strain gradients that cause fracture. However, where fracture is of concern, the reliance on simplistic models is primarily due to the lack of suitable stress/strain based fracture criteria to accurately evaluate the complex interactions of stresses and

strains. This is particularly the case when fracture occurs in structural components subjected to large-scale yielding and cyclic loading where traditional fracture mechanics approaches are not accurate. Moreover, many of these situations (especially those found in SCBFs) do not contain a sharp crack or flaw, which is another necessary assumption for the use of traditional fracture mechanics. Finally, earthquakes produce Ultra Low Cycle Fatigue (ULCF) in structures where very few (typically less than 10) cycles of extremely large magnitude (several times yield) are typical during the dynamic response of a building. This ULCF behavior is quite different from low or high cycle fatigue, which occurs in bridges and mechanical components. Consequently, continuum-based models that capture the fundamental physics of the fracture/ULCF phenomena are required to capture the complex stress-strain interactions leading to fracture. The continuum based models themselves are briefly presented in this report, however, a detailed discussion of these models can be found in Kanvinde and Deierlein (2004). These models simulate the micromechanical processes of ULCF to predict fracture from a fundamental physics-based perspective. They are fairly general, can be applied to a wide variety of situations as they work at the continuum level, and are relatively free from assumptions regarding geometry and other factors. Finally, these models require inexpensive tension coupon type tests for calibration (see Appendix A).

### 3.2. Comparison of Experimental Results with Continuum-Model Based Fracture Prediction

The images shown in Figure 3.2 compare deformed shapes from finite element analyses to those observed during the brace tests (Test #1 is shown here as a representative test). The comparisons demonstrate the ability of Finite Element Method (FEM) analyses to simulate local buckling and the localized regions of high stresses and strains where fracture is likely to initiate. The FEM analyses are performed with the commercially available software ABAQUS (1998) using continuum three-dimensional brick elements and multiaxial plasticity with large deformations.

Since triaxiality remains fairly constant during the cyclic loading history, the critical parameter that drives fracture is the plastic strain which is significantly amplified due to local buckling. It is important to note that there are two components to strain amplification between the global strain for the entire brace and the local strain that drives fracture. The first component is associated with the amplification of global longitudinal strains due to overall bending and global buckling of the brace. This bending strain is further amplified by the local buckling and of the cross section. Conventional beam-type analyses where the brace is modeled as a series of fiber-based beam column elements with an initial global imperfection (Uriz and Mahin, 2004) can simulate only the overall bending/buckling aspects of strain amplification. Continuum analyses (either brick or shell finite elements) are required to accurately capture the second component of stress and strain amplification due to local buckling. These amplified stresses and strains can then be used in physics based models to predict ductile fracture initiation in the steel braces.

 

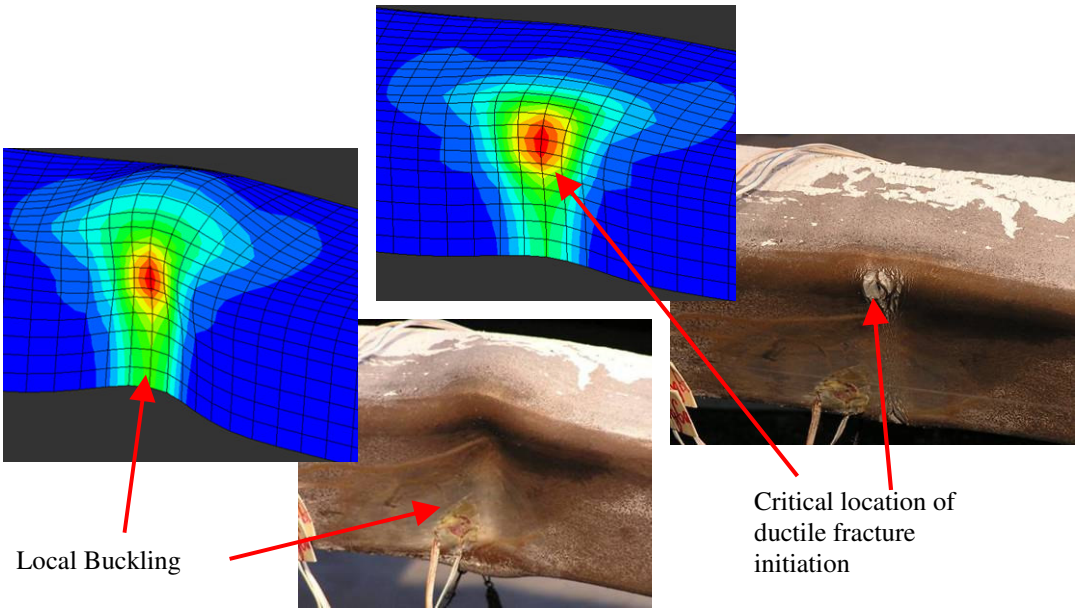


Figure 3.2: Comparison of local buckling (left) and fracture location

Ductile fracture and fatigue in steel is caused by the processes of void nucleation, growth, and coalescence (Anderson, 1995). As the steel material experiences a state of triaxial stress, voids tend to nucleate and grow around inclusions (mostly carbides in mild steels) in the material matrix and coalesce until a macroscopic crack is formed in the material. Previous research (Rice and Tracey, 1969) has shown that void growth is highly dependent on equivalent plastic strain, $e^p$, and stress triaxiality, $T = \sigma_m/\sigma_e$, where $\sigma_m$ is the mean or hydrostatic stress and $\sigma_e$ is the von Mises stress. Assuming that voids grow when the localized triaxiality is positive and shrink when this quantity is negative, Kanvinde and Deierlein (2004) quantified cyclic void growth – described by the ratio of the current void size, R, to the original void size, $R_0$ – with a modified version of the Rice and Tracy model for monotonic loading (Eq. 3.1.1) where $\psi$ is a coefficient that can range from 1.1 to 2.3.

$$\ln\left(\frac{R}{R_0}\right) = C\sum_{\substack{\text{tensile}\\ \text{cycles}}}\int_{e^p_{t_1}}^{e^p_{t_2}} \exp(\psi T)\, de^p_t \;-\; C\sum_{\substack{\text{compressive}\\ \text{cycles}}}\int_{e^p_{c_2}}^{e^p_{c_2}} \exp(\psi T)\, de^p_c \qquad (3.1.1)$$

For fracture to occur, the void growth demand should exceed the void growth capacity or critical void size $\eta_{cyclic}$. Under cyclic loading, the monotonic ductility measure, $\eta$, decays according to a damage law, which depends on another material parameter, $\lambda_{cyclic}$.

$$\ln\left(\frac{R}{R_0}\right)_{critical} = \eta_{cyclic} = \exp(-\lambda_{cyclic} e^p)\eta \qquad (3.1.2)$$

Since the demand (Eq. 3.1.1) and capacity (Eq. 3.1.2) are both expressed in terms of void size, these quantities can be plotted versus cycle number on the same set of axes in Figure 3.3. The figure depicts the evolution of the fracture prediction at the critical node (shown in Figure

3.2) for an HSS4x4x1/4 bracing member under the far-field loading history described in section 2.5.1. It is apparent that elastic behavior is observed prior to cycle 22 after which point the bracing member buckles globally. While the brace is far from ductile fracture initiation, this is the first sign of inelastic behavior both experimentally (see Figure 2.15a) and analytically. Similarly, local buckling was observed at cycle number 25.5 during both the experiment and ABAQUS simulation. Analytically, the damage that local buckling inflicts on the critical void size is marked by a significant drop in capacity (left plot of Figure 3.3) and a sharp increase in the demand/capacity ratio (right plot of Figure 3.3).

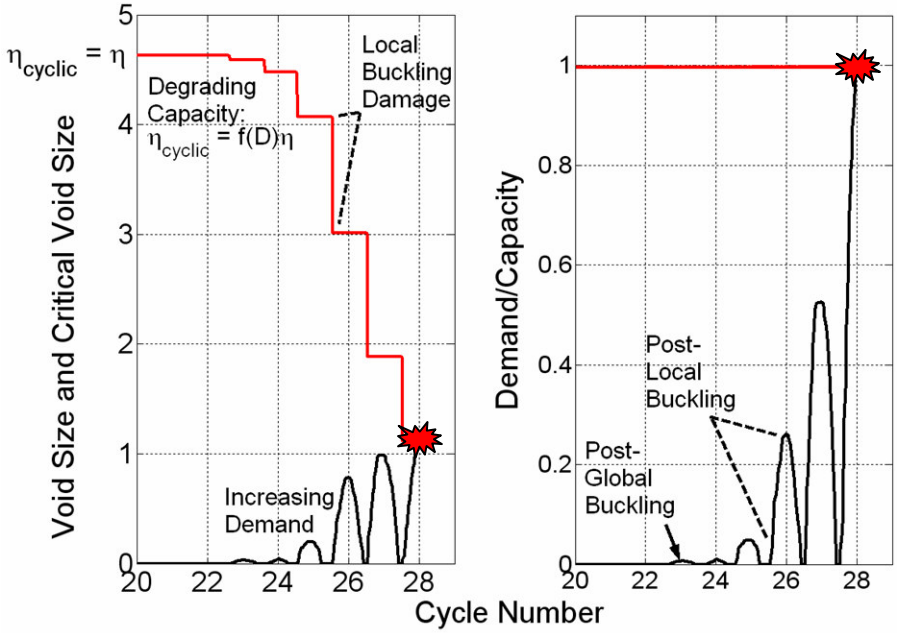


Figure 3.3: Fracture prediction evolution of Test #1 (HSS4x4x1/4)

Figure 3.4 compares the experimental and analytical hysteretic load-deformation curves. Two analytical curves are shown in the Figure; one is from a continuum analysis in ABAQUS and the second is a fiber-element-based analysis in OpenSees (2005). While both programs accurately simulate the load deformation behavior of the brace, OpenSEES cannot model the aforementioned local buckling modes that trigger fracture. Therefore, the stress and strain data from the critical location (shown in Figure 3.2) at the locally buckled cross section from the ABAQUS analysis is used to predict the time and location of ductile crack initiation (shown as a dot in Figure 3.4). A comparison of the analytical prediction to the experimental fracture instant (shown as an asterisk in Figure 3.4) demonstrates the accuracy of the ULCF models. Furthermore, as evident from Figure 3.2, the simulation predicts the critical location for ductile crack initiation with good precision.

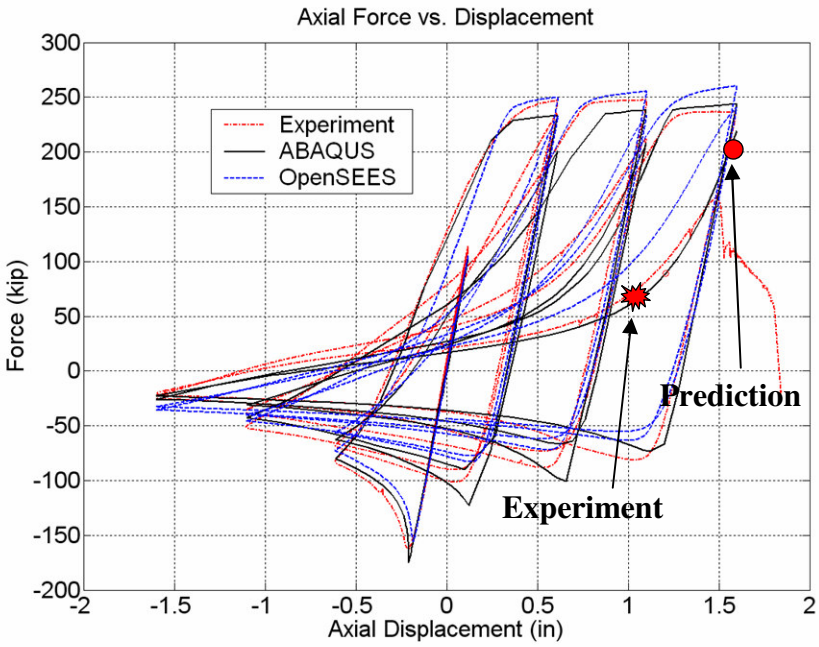


Figure 3.4: Force versus displacement comparison
(crack initiation prediction as dot and experiment as an asterisk)

### 3.3. Future Research Using FEM and Micromechanical Fracture Criteria

As discussed earlier, one of the most important advantages offered by these ULCF models is the insight into localized effects, and their relation to global geometric parameters that will inform design and detailing considerations. Some examples of where these models can be used to develop such insights are now summarized.

1. **HSS cold-worked corners** produce residual stresses and strains at the location of the bend that reduce the ductility of the section. Prior to this study, the fracture that initiates at the corners of HSS tubes was largely attributed to cold-working strains at that location. However, continuum-based fracture models predict that high strain demands caused by local buckling, rather than cold working, are more responsible for this type of failure. This is discussed in detail in section 4.3.

2. The **aspect ratio** (width to thickness) of reinforcing plates at the net section connection between the brace and gusset plate can be investigated by determining the ductility as a function of this ratio. This will provide designers with more information to ensure ductile connections in braced-frames.

3. **Slenderness**, **width-thickness**, and **cross sections** can be investigated through parametric studies to establish specific relationships between the ductility of the bracing member and these geometric descriptors. The experimental program suggests these trends; however, it is difficult to arrive at quantitative recommendations based on a limited set of data points. The continuum-based models can extend and generalize the set to situations beyond those that are experimentally investigated.

# 4. Design Implications

This chapter presents observations from the experimental testing program that directly pertain to structural design considerations for SCBFs. The effects of the cross section geometry, width-thickness ratio, buckling slenderness ratio, loading rates and histories, and other experimental queries and findings related to the specific limit state of fracture in bracing members are presented in a design context. The summary and Tables 2.4 and 2.5 presented in Chapter 2 are referred to in these discussions. Upon examination of the test data, significant trends are identified between geometric properties (such as the width-thickness of the cross section and slenderness of the member) and the ductility of braces and connections. While judging the observed performance of the experimental specimens (especially when improvements are suggested over current design procedures), it may be useful to note that the current design requirements for SCBFs (AISC, 2005) state that "braces could undergo post-buckling axial deformations 10 to 20 times their yield deformation". Given a yield level drift of approximately 0.3-0.5%, the Seismic Provisions could be interpreted as desiring a deformation capacity of approximately 3-5% for SCBF systems. While this seems large, one can use this as a point for comparison.

Each section in this chapter presents the rationale for studying a particular parameter (e.g. width-thickness ratio) and its likely effect on brace performance. For each parameter, observations and insights relevant to the performance of SCBF systems are then presented. Next, results from FEM analyses and ULCF fracture predictions (where available) are used to supplement the experimental findings to provide insights into localized effects that drive fracture initiation, thereby presenting the findings in a more general perspective. Finally, design implications of each of these observations are presented.

### 4.1. Effect of Width-thickness Ratios

As mentioned previously, fracture initiation in the central plastic hinge of bracing elements is driven by the amplified local strains induced by global buckling and more importantly, the local buckling of the cross section during reversed cyclic loading (see Figure 2.13). It is well established (Salmon and Johnson, 1996) that the onset of local buckling is controlled primarily by the section compactness, as governed by the width-thickness ratio and boundary conditions (e.g., stiffened or unstiffened) of cross section components. For the square HSS section the governing width-thickness ratio is b/t, where b is the clear inside dimension between the corner fillets and t is the wall thickness, for pipe the width-thickness ratio is D/t where D is the nominal outer diameter and t is the wall thickness, and for the W12 wide flange section the critical ratio is $b_f/2t_f$, where $b_f$ is the flange width and $t_f$ is the flange thickness.

Table 4.1 summarizes the width-thickness ratios for the various cross sections and the maximum permissible limits for the width-thickness ratios as per the AISC Seismic Provisions (2005). The last column of the table describes the width-thickness ratio of each section relative to these suggested limits and shows that the experimental program investigates a wide range of width-thickness ratios relative to the current AISC limits.

 

Table 4.1: Width-thickness properties of experimental braces

| Cross section | Width-thickness | Slenderness (K = 1.0) | $F_Y$* (ksi) | Width-thickness Limit # | $\frac{\text{width-thickness}}{\text{AISC Limit}}$ |
|---|---|---|---|---|---|
| HSS4x4x1/4 | 14.2 | 77 | 46 | $\frac{b}{t} \le 0.64\sqrt{\frac{E_s}{F_Y}} = 16.1$ | 0.88 |
| HSS4x4x3/8 | 8.46 | 83 | 46 | $\frac{b}{t} \le 0.64\sqrt{\frac{E_s}{F_Y}} = 16.1$ | 0.53 |
| Pipe5STD | 21.6 | 64 | 35 | $\frac{b}{t} \le 0.044\frac{E_s}{F_Y} = 36.5$ | 0.59 |
| Pipe3STD | 16.2 | 103 | 35 | $\frac{b}{t} \le 0.044\frac{E_s}{F_Y} = 36.5$ | 0.44 |
| W12x16 | 7.5 | 155 | 50 | $\frac{b_f}{2t_f} \le 0.3\sqrt{\frac{E}{F_Y}} = 7.22$ | 1.04 |

*Per ASTM; #As per AISC (2005)

### 4.1.1. Experimental Trends

Lower width-thickness ratios delay formation of local buckles, which in turn delays the onset of ductile fracture (due to the extreme strain gradients caused by the local buckles). Observations from the experimental program reaffirm that fracture can be significantly delayed by decreasing the width-thickness ratio of the cross section.

Test #1 and Test #4 provide a direct examination of this effect. The only difference between the specimen tested in Test #1 (HSS4x4x1/4) and Test #4 (HSS4x4x3/8) is the width to thickness ratios, where the HSS4x4x3/8 is significantly more compact (b/t = 8.46), as compared to the HSS4x4x1/4 (b/t = 14.2). In all other respects, i.e. slenderness, loading histories and material properties, the specimens are almost identical (see Table 4.1). Thus, Tests #1 and #4 can be used to directly assess the effect of width-thickness ratios on brace ductility.

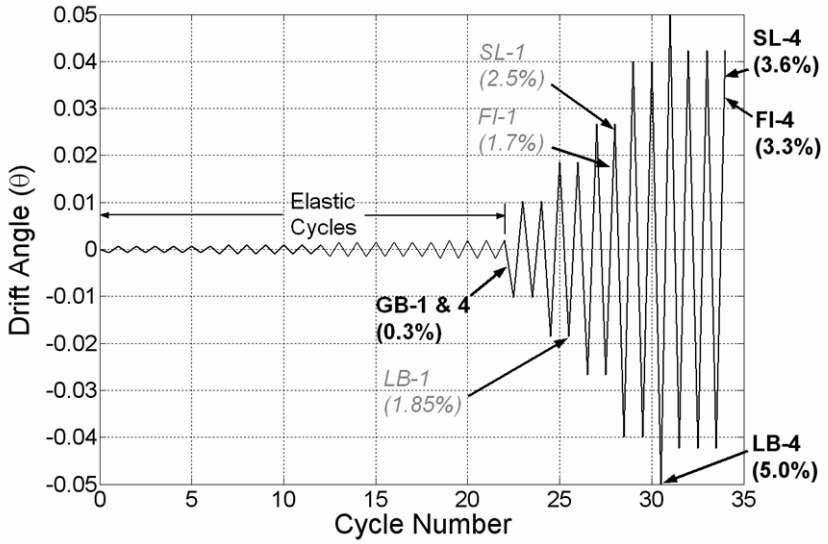

Figure 4.1: Comparison of *Test #1* with **Test # 4**

Figure 4.1 compares the important events of Tests #1 and #4. Although the global buckling (GB) drift of the two experiments is similar, local buckling (LB) was significantly delayed in the more compact section. The HSS4x4x1/4 brace sustained a maximum compressive drift of 1.85% before local buckles developed, while the more compact HSS4x4x3/8 brace

delayed local buckling to a 5% drift, an increase in ductility of approximately 170%. Accordingly, since the local buckles amplify strains to trigger fracture initiation (FI), the HSS4x4x3/8 specimen survived a tensile drift of 5% without crack initiation while the less compact HSS4x4x1/4 was only able to sustain a drift of 2.68% prior to fracture initiation. With a fracture endurance of 5%, the HSS4x4x3/8 provides an 87% ductility increase over the less compact HSS4x4x1/4. Strength loss (SL) occurred soon after fracture for both tests on the same loading ramp as crack initiation.

Similar trends are observed when comparing the Pipe3STD and Pipe5STD, where the 25% smaller width-thickness ratio of the Pipe3STD is consistent with more ductile behavior when compared to the Pipe5STD. Compared to the HSS tests, the PipeSTD sections provide a less direct assessment of the effect of width-thickness given that the larger slenderness ratio of the Pipe3STD (the more compact cross section) also contributes favorably to the ductility of the brace.

During far-field loading, the Pipe3STD showed an 87% higher ductility (5% maximum sustained drift) as compared to the Pipe5STD (2.68% drift). Interestingly, for the HSS specimens, a similar increase in ductility was achieved, albeit after a much larger reduction in width-thickness ratios (40% reduction for HSS, versus 25% for Pipe). Thus, in general, the performance of a brace is determined by a combination of member slenderness and cross section width-thickness ratios (Tang and Goel, 1989).

### 4.1.2. Design Implications

Referring to Table 4.1, both the HSS4x4x1/4 and Pipe5STD braces meet the current provisions (AISC, 2005) in terms of both slenderness and width-thickness ratios; however, each has a fracture and strength endurance of only 2.68% drift. Assuming a required inelastic drift capacity of 4% (i.e., twice the design story drift of 2%, as is commonly cited in performance testing requirements, such as for buckling restrained braces), neither of these two brace sections provides the expected deformation capacity. The 4% limit is met by the more compact HSS4x4x3/8 and Pipe3STD sections. This suggests that the maximum width-thickness limits in the AISC Seismic Provisions may be unconservative and should be reduced. Considering the idealized nature of the experimental setup to ensure precise boundary conditions and symmetric buckling behavior, a real structure may potentially exhibit less ductile behavior due to unsymmetrical effects (discussed in section 4.6). This further substantiates concerns that the currently specified width-thickness limits of the AISC Seismic Provisions (see Table 4.1) may not ensure the expected performance.

Additionally, since slenderness also governs the inelastic behavior of the member, it is not possible to view the width-thickness ratio in isolation. In fact, one could argue that the critical width-thickness ratio should depend on the slenderness ratio and the type of cross section to guarantee an acceptable fracture ductility of the buckling member. One can envision that the slenderness ratio be determined by the member or system level design considerations, while the critical width-thickness ratio could be considered a detailing issue, and expressed as a function of the slenderness to provide consistent ductility across various designs. For example, a more

 

slender member (indicative of elastic buckling) could afford a larger width-thickness ratio limit. To generalize such guidelines, parametric studies using the micro-mechanics based models can be performed to investigate the appropriate combination of width-thickness and slenderness limits for bracing members.

## 4.2. Slenderness Effects

In addition to the width-thickness of a cross section, the slenderness ratio ($KL_B/r$) also influences the performance of bracing members. As the slenderness increases, the compression member will exhibit elastic instead of inelastic buckling. Therefore, a stockier member (low slenderness) will show larger plastic strains at the center during cyclic inelastic buckling. Table 4.2 summarizes the slenderness data for all test specimens. The table also lists the maximum permissible slenderness ratio for each specimen. With the exception of the W12x16 member, the braces that were investigated as part of this experimental program were all within the slenderness limits listed in the AISC Seismic Provisions (2005). The table also reports other miscellaneous data, such as $\lambda$ and the ratio of maximum tensile to compressive loads.

Table 4.2: Slenderness properties of experimental braces

| Cross section | Slenderness (K = 1.0) | $F_Y$* (ksi) | Slenderness Limit (K = 1.0) # | $\lambda = KL_B / r\pi\sqrt{F_y/E}$ | $R_y F_y / F_{cr-R_y}$ |
|---|---|---|---|---|---|
| HSS4x4x1/4 | 77 | 46 | $\frac{KL_B}{r} \le 4\sqrt{\frac{E_s}{F_Y}} = 100$ | 0.98 (inelastic) | 1.8 |
| HSS4x4x3/8 | 83 | 46 | $\frac{KL_B}{r} \le 4\sqrt{\frac{E_s}{F_Y}} = 100$ | 1.06 (inelastic) | 1.9 |
| Pipe5STD | 64 | 35 | $\frac{KL_B}{r} \le 4\sqrt{\frac{E_s}{F_Y}} = 115$ | 0.69 (inelastic) | 1.4 |
| Pipe3STD | 103 | 35 | $\frac{KL_B}{r} \le 4\sqrt{\frac{E_s}{F_Y}} = 115$ | 1.12 (inelastic) | 2.3 |
| W12x16 | 155 | 50 | $\frac{KL_B}{r} \le 4\sqrt{\frac{E_s}{F_Y}} = 96$ | 2.0 (elastic) | 4.6 |

*Per ASTM; #As per AISC (2005)

### 4.2.1. Experimental Trends

Of the nineteen tests performed in this experimental study, no two tests had the same cross section with varying slenderness to enable a direct comparison based on the slenderness ratio. However, it is apparent from the results that slenderness is a controlling design parameter for bracing elements. For example, the most slender W12x16 showed the largest ductility across all three loading histories compared to the other four sections. The second most ductile brace was the Pipe3STD, which had the second highest slenderness ratio. Also, the experimental observations confirm that for a larger slenderness, the ratio between the maximum tensile and compressive strength increases and results in a larger overstrength factor for the system (compare last column in Table 4.2 to Table 2.5).

The W12x16 brace test, which exceeds both the width-thickness and overall slenderness limits prescribed by the AISC Seismic Provisions (refer Tables 4.1 and 4.2), illustrates the effect of slenderness on ductility. The relatively high width-thickness ratio of the W12x16 suggests a lower ductility, while the high slenderness ratio implies elastic buckling of the brace and a higher ductility.

Figure 4.2 depicts the significant events during Test #15 (W12x16, far-field loading history). Immediately apparent from the figure is the ductile behavior of the brace, despite the large $b_f/2t_f$ ratio. This suggests that local buckles cannot easily activate without the presence of a severe plastic hinge that develops during inelastic global buckling.

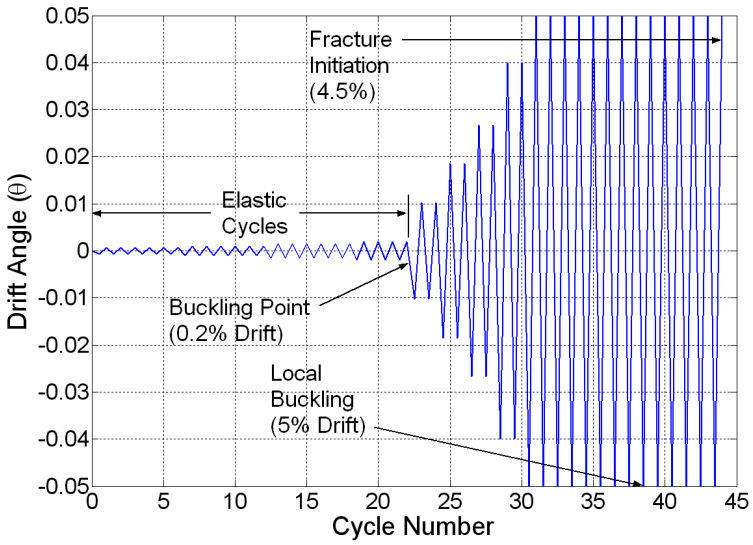


Figure 4.2: W12x16 experiment (far-field)

The performance of the PipeSTD sections can also be used to illustrate the influence of slenderness on ductility. As noted previously in section 4.1, the Pipe3STD was 61% more slender and 87% more ductile during far-field loading. The effect of slenderness can be further observed by comparing the far-field ductility increase of 87% to the equivalent increase described in section 4.1 for HSS. The HSS4x4x3/8 ductility increase, relative to the HSS4x4x1/4 performance, relied on a 40% more compact section (with constant slenderness) to achieve the 87% increase, while the Pipe3STD is only 25% more compact than the Pipe5STD suggesting that the higher slenderness of the Pipe3STD section also contributes to ductile behavior.

### 4.2.2. Design Implications

The W12x16 and PipeSTD tests show that elastic global buckling delays the formation of local buckling that is directly correlated with fracture. The wide-flange showed superior performance in terms of ductility compared to all of the other braces across all loading histories. Although higher slenderness ratios of bracing members result in more ductile systems, and may reduce drift demands, the negative economic aspects that accompany elastic buckling, such as increased overstrength factors or deficient energy dissipation, suggest that slender members may not always be desirable. Furthermore, since small slenderness ratios are unfavorable from a

 

fracture perspective, a braced-frame that combines small slenderness ratios with large width-thickness ratios should be avoided, while brace members with small width-thickness and moderate slenderness ratios are desirable. As discussed earlier, a practical means to incorporate the ductility enhancing effects of higher slenderness may be to establish width-thickness limits as a function of the slenderness of the member.

### 4.3. Influence of Cross section

While HSS members seem to be the most commonly applied brace type in SCBFs, pipe and wide-flange shapes hold potential advantages in terms of their fracture resistance. Moreover, architectural factors may limit the designer in the choice of cross section. It was for these reasons that the test matrix was designed to provide practical comparisons between these various shapes during earthquake-type loading.

#### 4.3.1. Experimental Trends

The previously shown local buckling modes (Figure 2.14) of the three experimental shapes – HSS, pipe, and wide-flange – are quite different in form and consequently, their ability to distribute the strain accumulation that triggers fracture is different as well. The qualitative differences of these experimentally observed buckles leads to differences in the manner of fracture in pipe and wide-flange members compared to HSS. Figure 2.14 illustrates the influence of the local buckling shapes on the fracture initiation pattern of the three experimentally investigated sections. Once the square HSS begin to form local buckles, the corners of the tube have the effect of amplifying the strains induced by local buckling. While the local buckles in the pipe and the wide-flange section also amplify the strains in the plastic hinge location, the strains are not as severe as those in HSS, mainly owing to the differences in cross sectional geometry and local buckling shapes.

#### 4.3.2. Design Implications

The large number of cycles between the onset of local buckling and fracture initiation for the W12x16 suggest that the local buckling mode shape of the W-section is somewhat less severe than that for the other cross sections. However, it is important to note that due to the large slenderness of the W12x16, the net plastic rotation demands at the hinge were smaller as well, thus one cannot make a general statement regarding the superiority of the wide flange shape. However, the pipe sections that were investigated showed more favorable fracture patterns compared to the HSS fractures that initiated at the corners. This suggests that locally buckled pipe sections do not lead to the sharp strain gradients seen in the HSS shapes and, therefore, show improved performance over the HSS shapes. Even with the drawbacks that the sharp corners of HSS present from a fracture context, based on the HSS4x4x3/8 test, HSS sections can provide the desired performance by limiting their width-thickness ratios (see Table 4.1).

One would also expect Round HSS to exhibit the more shallow strain gradients that were observed in the pipe sections. While Round HSS steel differs from that of pipe sections, the absence of sharp corners would most likely lead to the more favorable distribution of strains.

 

Since this was not directly investigated as part of this experimental study, one could envision the application of the methodology discussed in Chapter 3 to Round HSS members.

### 4.3.3. Effect of Residual Stresses and Strains from Cold-Working of HSS Tubes

Results from several experimental studies (Tremblay et al., 2005; Shaback and Brown, 2003; and Uriz and Mahin, 2004) show localized corner fractures in square HSS, resulting in the speculative theory that ductility is reduced due to the cold-working stresses introduced at the corners of these tubes. An interesting finding from this investigation through the use of the continuum-based fracture models suggest that the damage accumulated during cold working of the steel tube does not appear to decrease the capacity at the corner enough to drive fracture initiation at this location.

For the purpose of explanation, a Fracture Index will represent the results from the fatigue and fracture predictive models where stress and strain histories from finite element analyses are inputted into the ULCF model introduced in Chapter 3. This index will be used to express the proximity to fracture of a particular material point in the brace. Fracture initiation is predicted the instant that any point within the FEM mesh records a stress and cumulative strain state that drives the Fracture Index to unity. Since cold working creates residual stresses and strains in the steel, the fracture models are utilized to predict a reduction in capacity at the corner (labeled "Node 1" at the corner of an HSS4x4x1/4 cross section in Figure 4.3) of approximately 22% (Fracture Index $\cong$ 0.78). This reduced capacity (derived from plastic strain estimates due to cold working) at node 1 is represented by the dashed line in Figure 4.3, which describes the analyses results for two nodes within the finite element mesh. For comparative purposes, the second node is located at the midpoint of the cross section.

The far-field loading history discussed in section 2.5.1 is applied to the computer model to simulate the experimental boundary conditions. The results from the cyclic fracture prediction models (Figure 4.3) show the significant difference (far greater than the effect of cold working stresses) between the Fracture Index of node 1 and 2, which suggests that fracture in steel tubes is governed primarily by the demands that are created at the locally buckled corners, rather than by the cold working strains. This supports the work of Koteski et al. (2005) that showed annealing of steel tubes to reduce the residual stresses and strains that result from cold-working has a negligible effect on fracture performance.

 

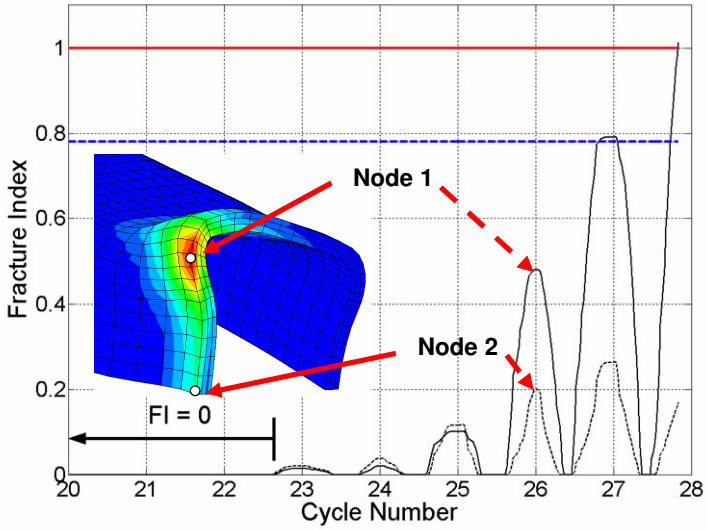


Figure 4.3: Fracture Index versus cycle number for HSS4x4x1/4 tube

## 4.4. Connection Performance

Hollow bracing members are often slotted at the end for attachment with the gusset plate (see Figure 2.4 and 4.4a). This results in a reduced area at the tip of the gusset plate where strains may concentrate to trigger net-section type fracture. While commonly used in construction, AISC (2005) does not permit the use of details in SCBF systems that might result in net-section type fracture. Recent studies, including a prior Steel TIPS report (Yang and Mahin, 2005), have suggested adding reinforcement plates at the reduced section to prevent fracture of this type (see Figure 4.4b). While Yang and Mahin conducted multiple tests to establish that the reinforcement plates mitigated the net-section fracture problem for square HSS, data to verify this is somewhat sparse for other types of cross sections. In fact, only one such test exists for pipe sections (Yang and Mahin, 2005), and no data exists for connections involving wide-flange braces and gusset plates (Figure 4.4c). To provide further data in this regard, the study described in this report investigated reinforced and unreinforced end details for pipe braces and end connection details for the wide-flange brace to examine this type of behavior.

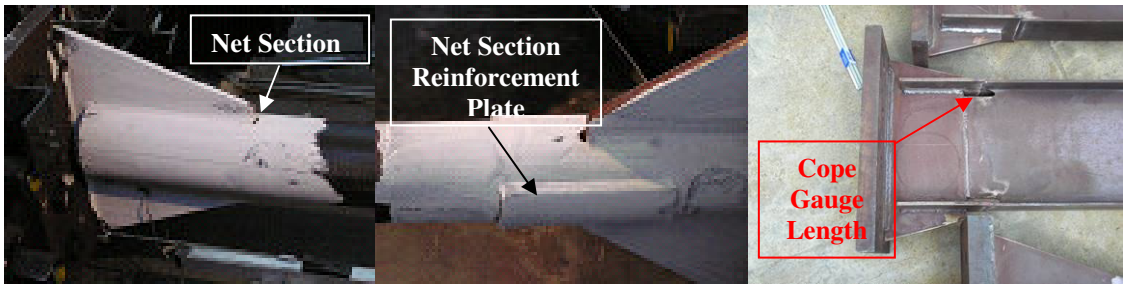


(a) (b) (c)

Figure 4.4: Representative brace connections of (a) Pipe5STD, (b) Pipe3STD, and (c) W12x16

### 4.4.1. Experimental Trends

Five tests (Test #s 8, 9, 10, 11 and 17) were designed specifically to examine these connection issues. These are summarized in Table 4.3 and 4.4 which show the maximum drift demands that each specimen sustained prior to failure and the comparison between experimental and predicted forces, respectively. The predicted maximum tensile forces are determined based on a variety of formulas, $R_yF_yA_g$, $R_tF_uA_g$, and $F_uUA_n$. This is to investigate the accuracy of the commonly used approach based on $R_yF_yA_g$, and compare it to other alternatives to predict maximum tensile brace force. An accurate assessment of the maximum tensile force is necessary to safely design the connection region without net section fracture or weld rupture.

Four of these tests featured pipe sections, two each Pipe3STD and Pipe5STD, one reinforced and one unreinforced. These were similar to the sections shown in Figures 4.4a and b. The fifth test was conducted on the connection between the W12 section and gusset plate, shown in Figure 4.4c. All the connections were detailed to prevent weld rupture under a maximum tensile force $R_yF_yA_g$. A tension dominated near-fault history (see Figure 2.12) was applied to each of these specimens. As discussed earlier, this loading history consisted of a large tension pulse followed by smaller cycles. The main intent of using the tension dominated near-fault history was to subject the connection region to the most severe demands possible. The other cyclic loading histories, with large compression cycles, tend to localize damage due to buckling at the center of the brace, thereby limiting the tensile demands that could develop at the net section. Therefore, it was critical to load the specimen with a large amplitude tension pulse before any cyclic damage accumulated in the center. If the brace survived the first large tension pulse, it would typically buckle and fail by fracture in the localized hinge at mid-length on subsequent cycles. Figures 4.5a and 4.5b show the Pipe3STD with and without reinforcement at the end of the experiments. The reinforced section shows minor yielding without fracture, whereas the unreinforced section fractures completely.

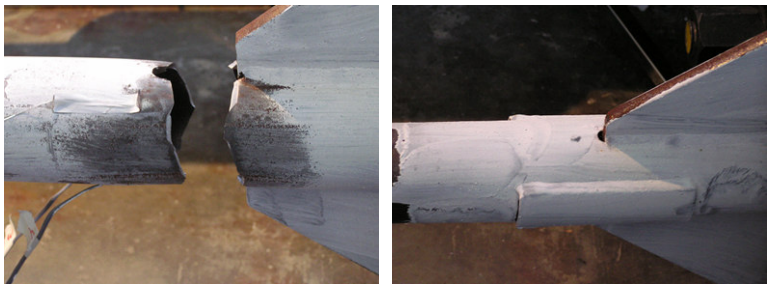

Figure 4.5: Pipe3STD connection performance after tensile excursion of (a) unreinforced and (b) reinforced net sections

Table 4.3 – Experimental results of bracing connections

| Test | Cross Section | Detail Type | Failure Type | Fracture/ Maximum Drift |
|---|---|---|---|---|
| 8 | Pipe3STD* | Unreinforced | Net section Fracture at end | 5.0% |
| 9 | Pipe3STD | Reinforced | Fracture in middle of brace | 8.0% # |
| 10 | Pipe5STD* | Unreinforced | Net section Fracture at end | 6.4% |
| 11 | Pipe5STD | Reinforced | Fracture in middle of brace | 8.0% # |
| 17 | W12x16 | NA | Fracture in middle of brace | 8.0% # |

*Failure at net section; #Denotes maximum drift sustained without fracture at net section. Failure occurred during the subsequent cyclic loading (refer Table 2.6 for details)

Table 4.4 – Experimental results of bracing connections

| Test | Cross Section | Detail Type | $P_{max}$ (kips) | $\frac{P_{max}}{R_y F_y A_g}$ # | $\frac{P_{2\%}}{R_y F_y A_g}$ # | $\frac{P_{max}}{F_u U A_n}$ | $\frac{P_{max}}{R_t F_u U A_n}$ ## | $\frac{P_{max}}{R_t F_u A_g}$ ## |
|---|---|---|---|---|---|---|---|---|
| 8 | Pipe3STD* | Unreinforced | 144 | 1.15 | 1.08 | 1.40 | 1.17 | 0.89 |
| 9 | Pipe3STD | Reinforced | 149 | 1.20 | 1.09 | NA | NA | 0.93 |
| 10 | Pipe5STD* | Unreinforced | 279 | 1.16 | 1.05 | 1.33 | 1.11 | 0.90 |
| 11 | Pipe5STD | Reinforced | 292 | 1.21 | 1.09 | NA | NA | 0.94 |
| 17 | W12x16 | NA | 323 | 1.25 | 1.16 | 1.41 | 1.28 | 0.96 |

*Failure at net section

# $R_y$ is 1.6 for pipe sections, 1.1 for W-section,

## $R_t$ is 1.2 for pipe sections, 1.1 for W-section (ASIC, 2005)

Referring to Table 4.3, one can readily observe that –

1. The unreinforced pipe sections exhibited net section type fracture, whereas the reinforced pipe sections survived deformations corresponding to drifts as large as 8.0% (during the first tensile pull of the near fault history) before buckling and fracturing at mid-length.
2. The unreinforced pipe sections fractured at deformations corresponding to drifts as large as 5.0% and 6.4% (the pipe test by Yang and Mahin sustained a drift of 4.9% prior to fracture, assuming a similar drift-deformation relationship).
3. The wide-flange section survived a drift of 8.0% without net section fracture before buckling and fracturing at mid-length on subsequent cycles. This may be attributed to the distribution of strains over a large gage length provided by the weld-access holes (see Figure 4.4c).

Beyond the five tests described in this section, it is relevant to note that the remaining tests, which were all reinforced HSS or pipe shapes (subjected to regular far-field or near-fault histories), did not exhibit any distress at their connections. This confirms earlier findings by Yang and Mahin (2005), which demonstrated the effectiveness of the net section reinforcement.

In the current AISC Seismic Provisions (2005), maximum tensile forces for connection design account for the common increase in yield stress of braces in tension (with respect to the ASTM minimum specified values) by amplifying $F_y A_g$ with an $R_y$ factor. The accuracy and conservatism of this approach is questionable since the measured force demands suggest that strain hardening plays a more significant role at increasing the force at relatively low drift levels. An alternate (upper bound) approach could involve using the $R_t$ factor which accounts for the increase from minimum specified to maximum expected ultimate strength ($F_u$), thereby including the effects of strain hardening.

It is reasonable to assume that the actual tensile demand on the connection will be bounded by the $R_y F_y A_g$ and $R_t F_u A_g$ estimates. In light of this, the experimental results are compared to both estimates. Section 4.4.2 considers the design implications of these observations and alternatives to estimate the maximum tensile force demand for SCBFs.

 

Referring to Tables 2.5 and 4.4 –

1. The maximum tensile forces predicted by the $R_yF_yA_g$ formula for the connection tests are, on average, 20% lower than the measured values, indicating that the $R_yF_yA_g$ formulas may be unconservative for calculating force demands on connections (Figure 4.6). The welds in the tests were designed based on these values, and likely did not fracture due to residual capacity afforded by the ϕ-factor.

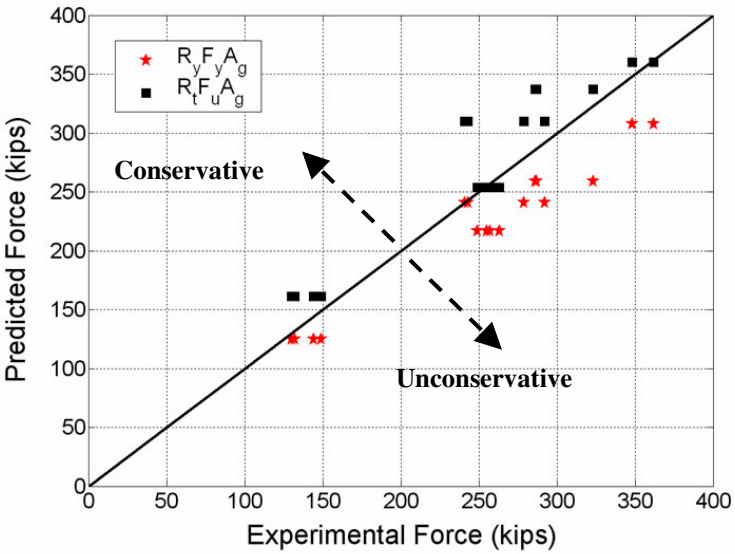

Figure 4.6: $R_yF_yA_g$ and $R_tF_uA_g$ predictions

2. A ground motion that subjects a brace to a large monotonic pull prior to any global buckling seems to be a fairly uncommon event considering the low drifts required to initiate buckling. Furthermore, analytical studies on SCBF systems suggest that design drift levels (10% in 50 events) are approximately 2% (Uriz and Mahin, 2004). Therefore, if one is concerned only with design level behavior, it might be more appropriate to compare the estimates with the peak tensile forces corresponding to the design level (2%) drift. Applying this approach to the PipeSTD specimens, Table 4.4 shows that the $R_yF_yA_g$ prediction is quite accurate and much more conservative (reduces from 20% to 8% above experimental). The W12x16 is still quite unconservative (reduction from 25% to 16%).
3. The maximum tensile forces predicted by the $R_yF_yA_g$ formula for the HSS braces (Table 2.5) are, on average, 17% lower than the measured values during far-field and compression near-fault loading histories (tension near-fault was not applied to HSS). This indicates that even during design level response the demands are significantly under-predicted and the connection details become solely reliant on the ϕ-factor to prevent failure, thus reducing the safety margin.

Table 4.5 lists the results for tensile coupon tests from the brace specimens and helps explain the reason for the unconservative nature of the $R_yF_yA_g$ prediction for the HSS, as well as the more accurate PipeSTD predictions at design drift levels (2%). It is apparent that the yield stress for the PipeSTD steel (47.5 and 54 ksi) is less than the expected value according to currently published $R_y$ values, while the HSS yield stress (70.3 – 79.5 ksi) is larger than the maximum expected. Thus, the HSS brace steel is somewhat of an outlier, with a higher than expected yield stress and lower than expected ultimate stress. Without further substantiating statistical data, it is difficult to draw firm conclusions about the appropriate values and criteria to use in design.

Table 4.5: Measured material properties from coupon tests (see Appendix A)

| Specimen | Steel | Measured $F_y$ (ksi) | Measured $F_u$ (ksi) | Measured $R_y$ (AISC $R_y$) | Measured $R_t$ (AISC $R_t$) |
|---|---|---|---|---|---|
| HSS4x4x1/4 Corner | A500 Gr. B | 73.5 | 80.8 | 1.6 (1.4) | 1.4 (1.3) |
| HSS4x4x1/4 Center | A500 Gr. B | 70.3 | 74.3 | 1.5 (1.4) | 1.3 (1.3) |
| HSS4x4x3/8 Corner | A500 Gr. B | 73.5 | 79.2 | 1.6 (1.4) | 1.4 (1.3) |
| HSS4x4x3/8 Center | A500 Gr. B | 79.5 | 88.5 | 1.7 (1.4) | 1.5 (1.3) |
| Pipe3STD Longitudinal | A53 Gr. B | 54.0 | 66.8 | 1.5 (1.6) | 1.1 (1.2) |
| Pipe5STD Longitudinal | A53 Gr. B | 47.5 | 62.4 | 1.4 (1.6) | 1.0 (1.2) |

4. Using the $R_tF_uA_g$ formula (AISC, 2005), based on the ultimate strength of the material, provides fairly accurate and slightly conservative estimates of the maximum tensile capacity of the bracing members.
5. The net-section capacity formula $F_uUA_n$ is conservative by approximately 40% while predicting the tensile load capacity of the member. Using $R_tF_uUA_n$ reduces the conservatism of the estimate to approximately 20%.

### 4.4.2. Design Implications

Based on these findings, one can make some preliminary observations that have implications regarding the design of these connections.

1. Reinforcing the pipe sections prevents fracture at the reduced section even at deformations corresponding to extremely large drifts (≈ 8%)
2. Even the unreinforced pipes sustain fairly large deformations (≈ drifts of 5-6%) before fracture. This is probably due to strong hardening observed in the pipe sections allowing for the redistribution of stresses in the net section.
3. The wide-flange section, owing to the large gage length of the reduced section (length of the weld cope hole – see Fig. 4.4c), exhibits large ductility (≈ 8% drift).
4. While the $R_y$ factor reflects the variability in the yield point of steels, it does not reflect the stress increase due to hardening, or the variability in the ultimate strength. While hardening might be advantageous in terms of load capacity, it can place excessive tensile force demands on the detail (welds or net section). Furthermore, if the steel greatly exceeds the ASTM minimum specified yield stress then $R_yF_yA_g$ can under-predict the tensile demands on the connections and, therefore, decrease the reliability of the connection. This was the case with the HSS braces, and to some extent, the W12x16 specimens.
5. Rare ground motions could also create excessive demands on connections that $R_yF_yA_g$ can not account for. An example of this is the near-fault tension tests on four PipeSTD braces and one W12x16.
6. Across all brace tests and materials, the formula $R_tF_uA_g$, based on ultimate strength of the material is found to provide an accurate (and slightly conservative) upper bound on the tensile load capacity. Although the predictions using $R_tF_u$ in Table 2.5 seem over-

conservative (6 to 12% above observed) for the far-field PipeSTD experiments, this is explained by the fact that the yield and ultimate stresses of this steel sample are less than the expected values.

While it is apparent that reinforcing plates are essential for ductile connection performance, the conclusions present a designer with a difficult choice concerning the force capacity of SCBF connections, e.g. weld detail. Several possible solutions are:

1. Design with $R_yF_yA_g$ as per AISC (2005). The advantage is a decreased design force when compared to alternatives (3) and (4). The drawback is the unconservative nature of the prediction due to rare ground motions (large pulses and events larger than 10/50), structural response, and the statistical probability of encountering steel materials with larger than expected yield strengths.
2. Restrict $F_y$ on structural plans and design with $R_yF_yA_g$. Again, the benefit is the smallest design force when compared to the following alternatives. However, this could be problematic and more expensive for fabricators since they are not able to control the steel shipments from the mills.
3. Design with $\alpha R_yF_yA_g$ where $\alpha$ is an amplification factor to account for hardening of the various steels used in SCBF construction during design level or rare events. Tremblay (2002) has employed this approach with $\alpha = 1.1$ for HSS sections. The disadvantage is the larger design forces that would result from this formulation and the need to research proper $\alpha$ factors to be used in design.
4. Design with $R_tF_uA_g$. The apparent benefit of this approach is the conservative nature of the maximum tensile demand prediction. From the perspective of this experimental study, $R_tF_u$ is the most conservative estimate, even in light of the large yield stress of the HSS steel and rare loading conditions placed on several PipeSTD and W12x16 braces. The disadvantage is the largest design forces of the presented alternatives.

### 4.5. Rate Effects

Two cyclic loading tests (Test #3 and 5) are conducted at high-loading rates comparable to earthquake loading rates. High loading rates can affect fracture ductility through two independent mechanisms. First, higher loading rates and the associated high strain rates induce elevated stresses due to rate-dependent material behavior (illustrated schematically in Figure 4.7). These elevated stresses may reduce ductility by triggering stress-dependent fracture mechanisms such as cleavage. Second, the higher loading rates do not allow thermal dissipation and cooling during loading (as would be the case in slower tests). Consequently, the temperatures in the regions of high localized strain can be elevated substantially in the high-rate tests. It is well known that higher temperatures increase the ductility of steel (Figure 4.8), such that material

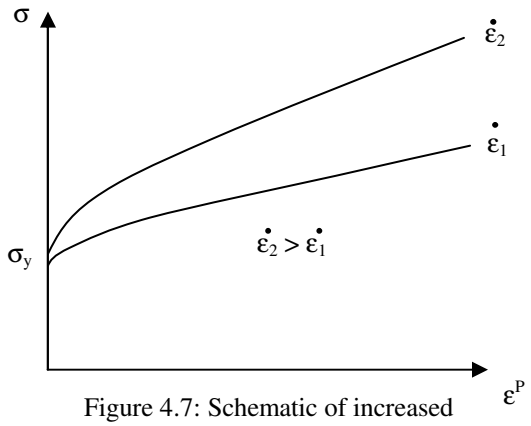

Figure 4.7: Schematic of increased stresses due to larger strain-rate

behavior transitions from brittle to ductile fracture with rising temperature. Therefore, increasing the loading rates can have adverse as well as beneficial impacts on fracture ductility. The relative dominance of these effects is a function of specimen geometry, stress constraint, the presence of cracks, as well as material properties. Thus, without conducting experiments, it is somewhat difficult to assess the effects of loading rates on fracture ductility. A comparison of response under different strain rates allows for the transfer of results from typical quasi-static experiments (that are common in literature) to earthquakes, where loading is applied at a high rate. Experimental findings based on the tests discussed in this section confirm that for many situations of practical interest, this is, in fact a legitimate approach.

### 4.5.1. Experimental Trends

Two brace specimens were subjected to earthquake rate loading that applied the far-field loading history at a higher rate than the other experiments. The intent was to compare Test #1 and Test #3 (HSS4x4x1/4 specimens) and Test #4 and Test #5 (HSS4x4x3/8) – refer Table 2.6 – to determine if the increased strain-rate and temperature affects fracture initiation.

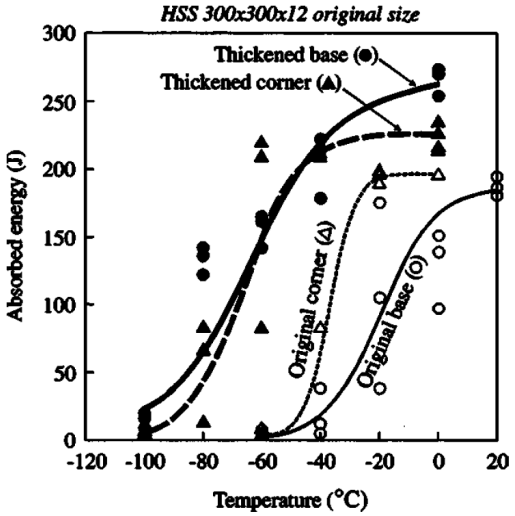

Figure 4.8: Charpy-v-notch curves (Koteski et al., 2005)

The earthquake loading rate was determined using the approximate secant stiffness at the design drift and corresponding elongated period of the chevron braced frame in Figure 2.9. These calculations resulted in a rate of 6.0 in/sec for each loading excursion, which is 360 times faster than the slow rate of 1.0 in/min used in the other tests. Note that using multiple dynamic analyses to capture the exact earthquake rate is time intensive and unnecessary in the context of this investigation; rather using a rate that is approximately the same magnitude of a realistic event serves the purpose of this project by presenting a sufficient comparison of performance between quasi-static and real time testing.

Unfortunately, the actuators could not be controlled accurately at the high loading rate, resulting in over-shooting of the displacement limits. The inconsistent displacement limits make it somewhat difficult to judge if the increased strain rate or temperature in the region of fracture had a substantial effect on the performance of the brace. However, after both experimental histories are input into an FEM model of the brace and fracture initiation is predicted with the ULCF models (described in chapter 3), the resulting deviations between the prediction and the experiment are essentially the same for both tests. Therefore, within the precision of the models, rate effects do not seem to affect fracture significantly.

Additionally, with reference to Charpy-V-Notch curves (shown in Figure 4.8 for HSS12x12x1/2 specimen from work of Koteski et al., 2005), the authors believe that the flaw-free geometry of the braces, due to their low-stress constraint would result in ductile, upper-shelf

 

behavior, rather than brittle behavior. To support this claim, thermo-couples were placed at the midpoint and at locations slightly offset from the midpoint to observe the manner of thermal dissipation during slow and fast rate loading. The maximum recorded temperature on the surface of the HSS4x4x3/8 brace for an earthquake rate test was 200°F compared to the 91°F reading during the slow HSS4x4x1/4 test. This data is supplied more for a qualitative perspective to support the conclusion that loading rate does not influence fracture initiation in the braces. Since the Charpy curves plateau after a critical temperature (i.e., between -40°C (-104°F) and 20°C (68°F) in Figure 4.8) is reached, moving from 91°F to a recording of 200°F does little to affect the ductility of fracture in the brace.

### 4.5.1 Design Implications

The comparison between fast and slow strain rate tests shows that quasi-static testing can appropriately reproduce the fracture response of flaw-free structures during earthquake rate loading. Therefore, these tests may be used to support other previous and ongoing experimental work that typically uses quasi-static testing.

Furthermore, for the flaw-free geometry of SCBF braces the increased rate effect does not have a significant, observable impact on cyclic ductility. This allows extrapolation of the micromechanical-based models to predict fracture of full-scale members and connections during actual seismic events.

## 4.6. Effect of Unsymmetrical Buckling

Several of the experiments performed during this testing program showed unsymmetrical buckling patterns involving formation of a plastic hinge away from the center of the brace. This behavior led to a loss of ductility when compared to members that demonstrated symmetric buckling. This may be due to the larger strains that are developed (due to the kinematics) when the plastic hinge is not at the center of the brace.

### 4.6.1. Experimental Trends

To serve as a control, Test #6 and Test #7 are essentially identical Pipe3STD specimens that showed fracture initiation on the same tensile ramp and both formed local buckles at the midpoint of the member (see Table 2.6).

On the other hand, the comparison between Test #12 and Test #13 – both Pipe5STD braces subjected to far-field loading – show unsymmetrical buckling of the brace in Test #13 and also a lower fracture ductility compared to Test #12 which survived an additional cycle at 2.68% drift and buckled symmetrically. This unsymmetrical buckling can likely be attributed to minor fabrication imperfections or boundary condition changes in the experimental setup and was not expected prior to the tests.

To further investigate this response, Test #19 had two 18” reinforcing plates welded at the center to the top and bottom (non-buckling faces) of the brace to deliberately induce

 

unsymmetric buckling. In all other respects, the specimen was similar to Test #1. As expected from the Pipe5STD comparison, the ductility decreased by 31% from a maximum sustainable drift before fracture of 2.68% in Test #1 (symmetric) to 1.85% in Test #19 (Figure 4.9). The welded attachment is not believed to influence fracture substantially (other than by causing the non-symmetric buckling pattern) since fracture initiation began approximately two inches from the end of the reinforcing plate (see Figure 4.9).

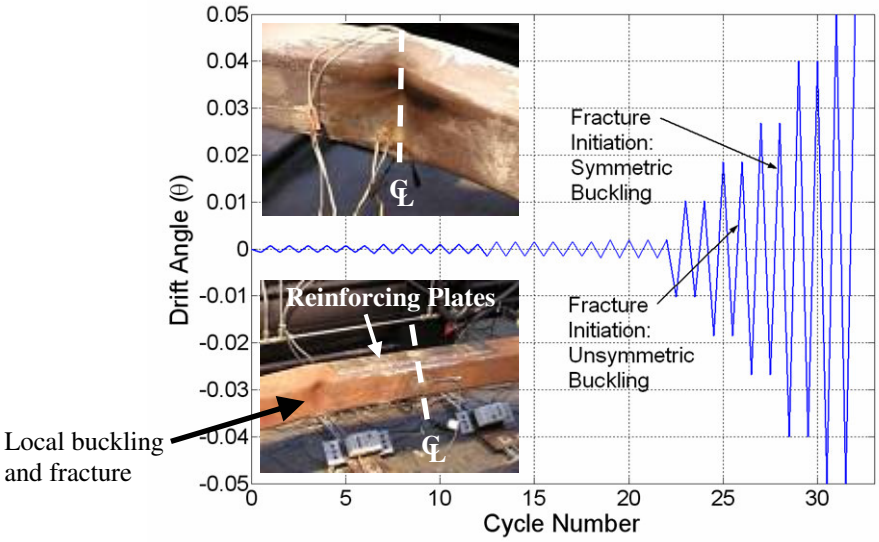


Figure 4.9: Test #1 and Test #19 (bottom picture) comparison

### 4.6.2. Design Implications

The comparison of Tests #1 and 19 highlight the extent to which non-ideal conditions may affect the response, which is an important point to be considered while interpreting test results from specimens that are idealized representations of conditions in actual buildings. As demonstrated in this comparison, imperfect boundary or loading conditions that lead to unsymmetric buckling will likely cause larger localized strain demands as compared to those in idealized cases where hinges form in the middle of the brace. The larger strain demands will in turn hasten the onset of fracture. The extent to which these non-ideal conditions will impact actual building response is uncertain. The extent to which unloaded attachments, such as the plates in Test #19, can affect response supports the requirement of a protected zone that is currently in the code for design (AISC, 2005) of SCBF systems which guards the lateral load resisting elements against nonstructural factors that could change or hinder the desired response.

## 4.7. Concrete Filled Braces

Previous experimental investigations have shown that concrete filled tubes may exhibit higher ductility and withstand more cycles of reversed loading compared to their equivalent hollow sections (Liu, 1988). This is due to the ability of the confined concrete inside the tube to delay local buckling and the accumulation of strain that drives fracture initiation. Even when local buckling occurs in concrete-filled tubes, the tubes tend to buckle outward because of the

presence of the concrete, and the longer buckle-wavelength associated with this mode may reduce the strain demands in comparison to the short wavelength inward-buckling for unfilled tubes (see Figure 4.10).

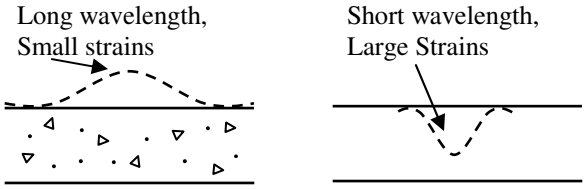


Figure 4.10: Schematic comparison of concrete filled HSS tube local buckle (left) to hollow section

### 4.7.1. Experimental Trends

Two HSS4x4x1/4 braces were filled with high strength cement ($f_c$' 6-8 ksi) to investigate the effect on performance. One of the concrete specimens (Test #17) was subjected to a far-field loading history and is compared with the results from Test #1 while the other (Test #18) was subjected to a compressive near-fault history and compared with Test #2. These specimens were similar in all other respects.

During Test #17, the largest sustained tensile drift was a 2.68% drift, which is also the largest sustained during Test #1 suggesting that the concrete fill does not benefit performance (Appendix B shows that even though the maximum drift levels are the same, the concrete filled tube fractures on the subsequent tensile excursion after the hollow tube in Test #1). However, since Test #1 with the hollow section formed the local buckle at the midpoint, the discussion presented in section 4.6 suggests this may not be a consistent comparison due to the influence of the more pronounced unsymmetrical buckling that occurred with the concrete filled tube shown in Figure 4.11. Nevertheless, these data do call into question the effectiveness of concrete fill to improve brace response.

The comparison of the concrete filled tube to the hollow tube subjected to near-fault compression histories (Test #2 versus Test #18) shows a significant increase in ductility (see Table 2.6 or Appendix B).

### 4.7.1. Design Implications

From a construction perspective, concrete-filled tubes present logistical challenges for general contractors and their subcontractors. However, previous research has suggested that concrete fill can delay local buckling and hence fracture. The two tests conducted with concrete fill in this program were inconclusive as to whether there is a distinct improvement in response with concrete fill. On the one hand, the tests under far-field loadings did not show much improvement with fill, whereas the tests conducted under a pulse-like near-fault response did show an improvement. However, the advantages that concrete filled steel tubes present may be achieved by using more compact sections to delay local buckling or alternative cross section

 

shapes (pipe or wide-flange) that delay fracture. For example, section 4.1 illustrated the effect of a lower width-thickness ratio on the more ductile HSS4x4x3/8 compared to the HSS4x4x1/4.

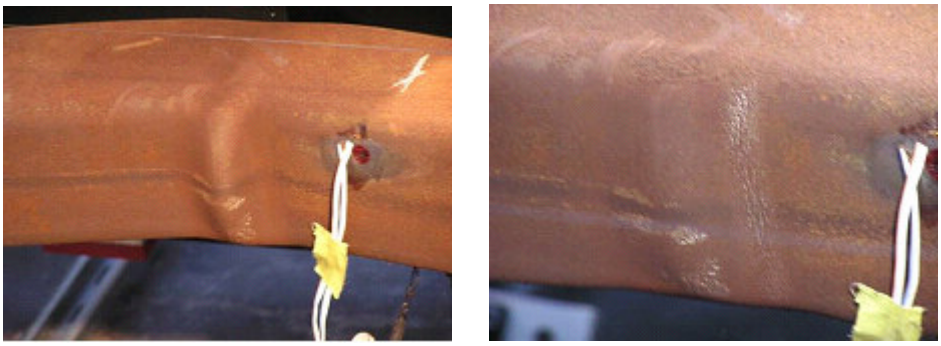

Figure 4.11: Outward local buckling (left) and fracture in a concrete filled tube

# 5. Summary

This report presents findings and design implications based on nineteen large scale tests of bracing elements subjected to earthquake type cyclic loading. The research described is part of a NEESR (Network for Earthquake Engineering Simulation and Research) project that aims to validate fundamental fracture and Ultra-Low Cycle Fatigue (ULCF) models for steel structures. This report focuses specifically on the practical design implications of the experimental program.

The experiments feature brace specimens detailed as per current code, and subjected to various types of cyclic loading histories designed to replicate realistic seismic demands. The testing matrix included a diverse blend of parameters including cross section width-thickness, slenderness, type of cross section, loading history, loading rate and special details such as concrete filled braces. Various limit states, such as local buckling, fracture initiation and loss of strength were monitored, and related to system level drift levels.

The braces subjected to cyclic loading failed due to fracture at the center, which was triggered by strains highly amplified due to local buckling. Consequently, cross section width-thickness ratios were found to strongly influence brace ductility for all cross sections, and higher width-thickness ratios resulted in a severe decrease in ductility. Importantly, in some experiments with low slenderness ratios, current AISC limits for width-thickness ratios could not ensure acceptable performance, resulting in fracture at unacceptably low drift deformation levels (2-3% drifts).

Apart from width-thickness, slenderness was determined to be another important factor affecting brace fracture, in that more slender braces suffered relatively lower levels of inelasticity, delaying fracture. In fact, fracture itself was found to be governed by a combination of slenderness and width-thickness. For example, the wide-flange section with an undesirable width-thickness ratio exhibited excellent ductility, likely because of its high slenderness. However, large slenderness can reduce energy dissipation in the brace, and place excessive tensile demands on connections (due to overstrength). Since brace slenderness is a system level

design variable, it might not be feasible to provide large slenderness with the sole intent to prevent fracture. On the other hand, the beneficial effects of large slenderness may be leveraged to adjust limits on width-thickness ratios, recognizing that fracture is in fact governed by a combination of the two factors.

In addition to slenderness and width-thickness, various other factors were considered. Of these, the type of cross sectional shape (HSS, pipe or wide-flange) was found to affect ductility. The square HSS were found to be particularly susceptible to fracture due to their specific local buckling shape, which greatly amplifies strains at the corners. In contrast, the pipes and wide-flange showed more gradual local buckling shapes resulting in greater ductility. Filling the braces with concrete resulted in a somewhat larger ductility in one of two tests, but given the logistical challenges to this, one could achieve similar levels of ductility by using either a more compact shape or an alternate cross section. Rate effects were examined and determined to be relatively unimportant, especially for the flaw-free braces discussed herein.

Connection performance regarding net section fracture at slotted brace-ends was investigated by subjecting these to tension dominated near-fault loading histories with a large initial tensile pulse. These tests, conducted for pipe sections and one wide-flange section, confirmed previous findings that net section reinforcement increases ductility substantially and prevents fracture at the connection. In fact, for the pipe specimens, the large difference between yield and ultimate strengths resulted in large ductilities even for unreinforced connections. Overall, the variations in the expected versus nominally specified material properties demonstrate the degree to which the net section fracture response may differ between different structures. The test data did confirm that the expected yield strength ($R_yF_yA_g$) and the expected ultimate strength ($R_tF_uA_g$) tend to bracket the maximum measured strength fairly well.

While not discussed at length in this report, the experimental study was successful in its primary aim, which was to validate the micromechanics-based fracture and fatigue models. These models can be used to understand localized fracture effects and to generalize the findings of the experimental study with parametric analytical studies. Examples that demonstrate such use of these models are provided in this report. These advances in modeling, along with future research focusing on weld metals, will reduce the reliance on experiment-based research and provide a useful research tool for studying design requirements for fracture-critical structures.

 

## Appendix A: Material Properties

Material properties used in the continuum-based and line element models of the braces, as well as in the fracture initiation predictions, were determined by extracting small-scale test specimens from representative sections that the steel fabricator provided. Longitudinal coupons were extracted from both PipeSTD sizes, while center and corner coupons were extracted from HSS specimens (Figure A.3 and A.4). Coupons were not extracted from the W12x16 specimen. However, the work of Kanvinde and Deierlein (2004) provides accurate material data for the steel that is commonly used in wide-flange sections and the authors plan on verifying this data with coupons from the fractured full-scale specimens.

Figure A.2 shows the dimensions of the tensile coupons that were used to determine the uniaxial stress-strain constitutive relationships.

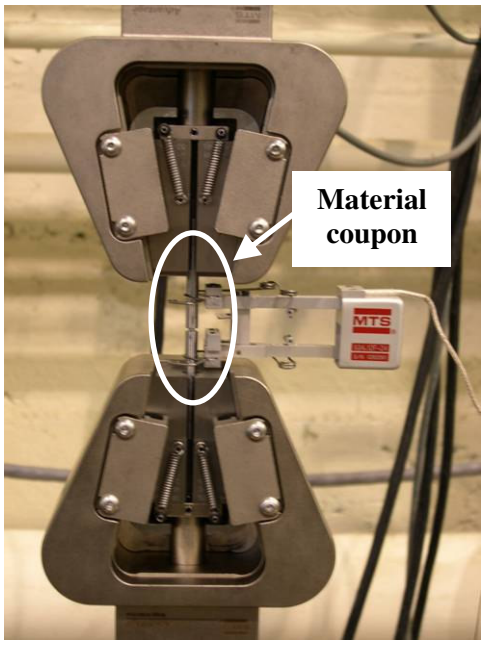


Figure A.1: Experimental setup

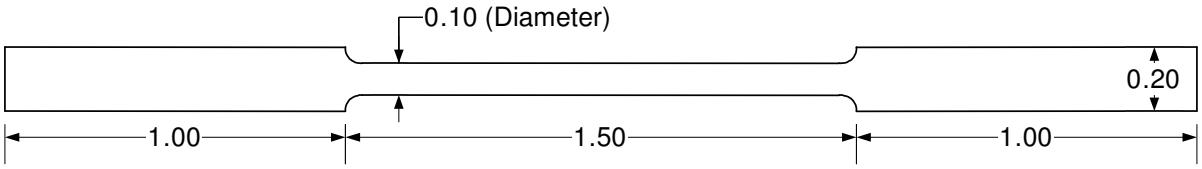


Figure A.2: Coupon geometry (dimensions in inches)

All specimens were tested monotonically to fracture under displacement control. The load was measured using a 3-kip load cell while the strain was measured using an extensometer with initial gage length of 1.0" (Figure A.1). To determine the ductility of the material, the diameter of the necked fracture surface was measured and compared with the initial diameter.

The results from the tensile coupons are summarized in Table A.1. Plots of typical stress-strain behavior from the HSS and PipeSTD coupons are shown in Figures A.3 and A.4, respectively.

Table A.1: Material properties from monotonic coupon testing

| Specimen | Steel | Elastic Modulus, E (ksi) | Yield Stress, $F_y$ (ksi) | Ultimate Stress, $F_u$ (ksi) | Fracture Strain, $\varepsilon_F$ (in/in) | Hardening Exponent, n |
|---|---|---|---|---|---|---|
| HSS4x4x1/4 Corner | A500 Gr. B | 29300 | 73.5 | 80.8 | 0.11 | 0.05 |
| HSS4x4x1/4 Center | A500 Gr. B | 30900 | 70.3 | 74.3 | 0.13 | 0.05 |
| HSS4x4x3/8 Corner | A500 Gr. B | 29400 | 73.5 | 79.2 | 0.09 | 0.05 |
| HSS4x4x3/8 Center | A500 Gr. B | 27100 | 79.5 | 88.5 | 0.11 | 0.04 |
| Pipe3STD Longitudinal | A53 Gr. B | 31500 | 54.0 | 66.8 | 0.20 | 0.11 |
| Pipe5STD Longitudinal | A53 Gr. B | 31400 | 47.5 | 62.4 | 0.15 | 0.13 |

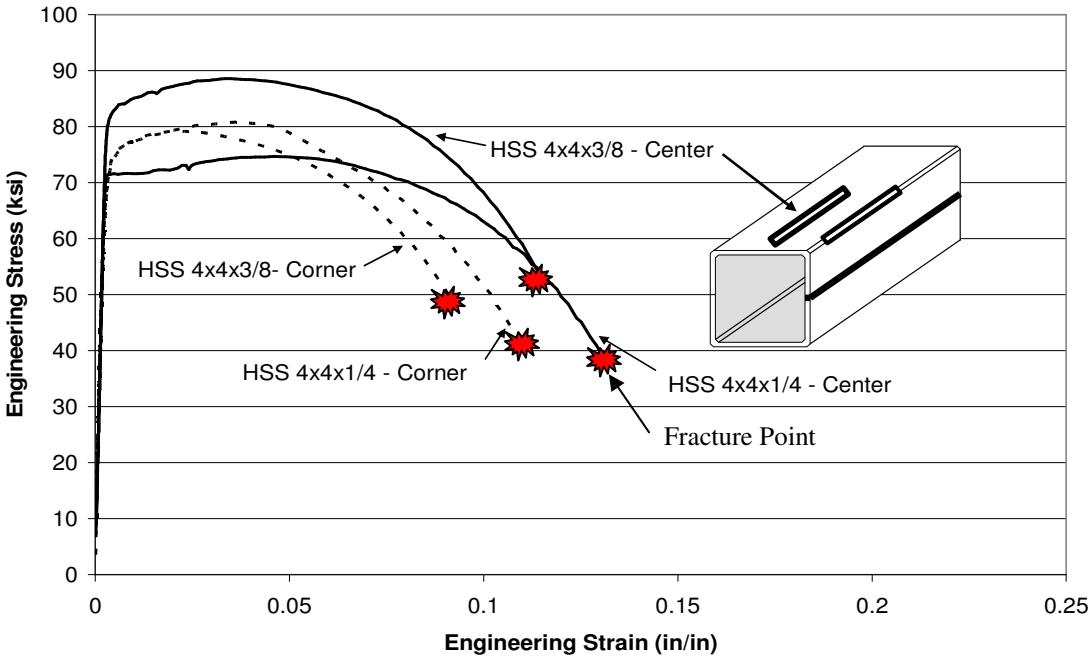


Figure A.3: Monotonic stress-strain plot for HSS coupons

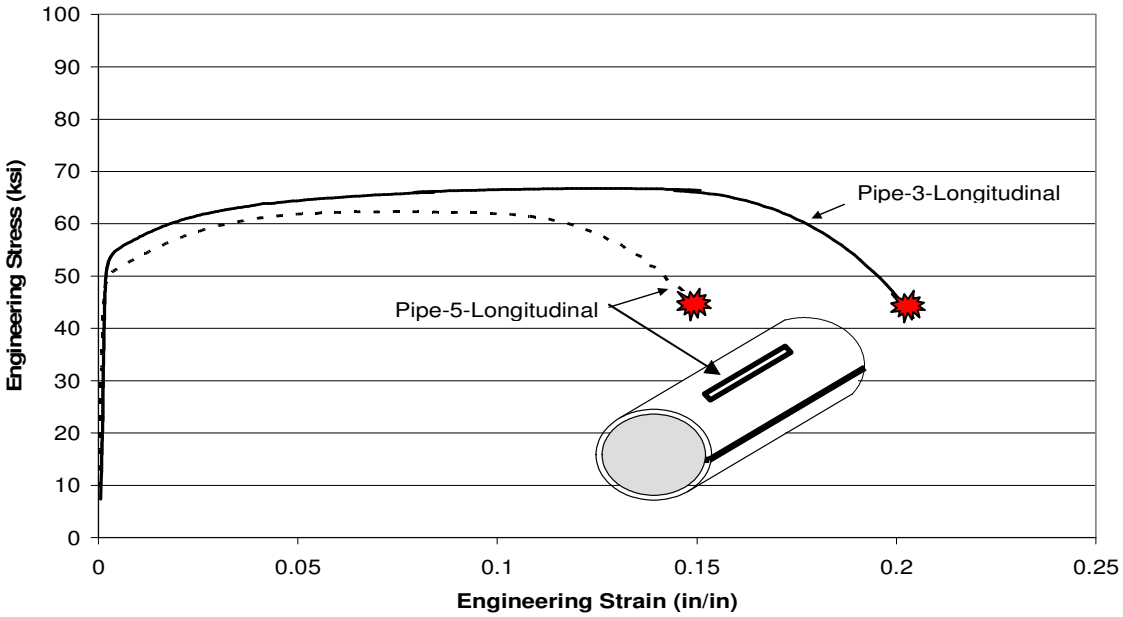


Figure A.4: Monotonic stress-strain plot for PipeSTD coupons

 

## Appendix B: Experimental Hysteretic Plots and Backbone Curves

Figure B.1 illustrates the loading histories and load-deformation plots for each of the nineteen braces. The significant limit states are reported on each figure, while the stiffness and maximum tensile and compressive forces are shown on the hysteretic plots. The test numbers correspond to Table 2.1 and titles are also provided in this section to distinguish and compare the specimens, loading histories, and other experimental attributes.

Theoretical backbone curves for simulation are developed. These depend on fundamental material properties as well as geometric properties of the cross section and the bracing member. For several experiments, these nonlinear tension and compression backbones are compared to the experimental results to validate the methodology.

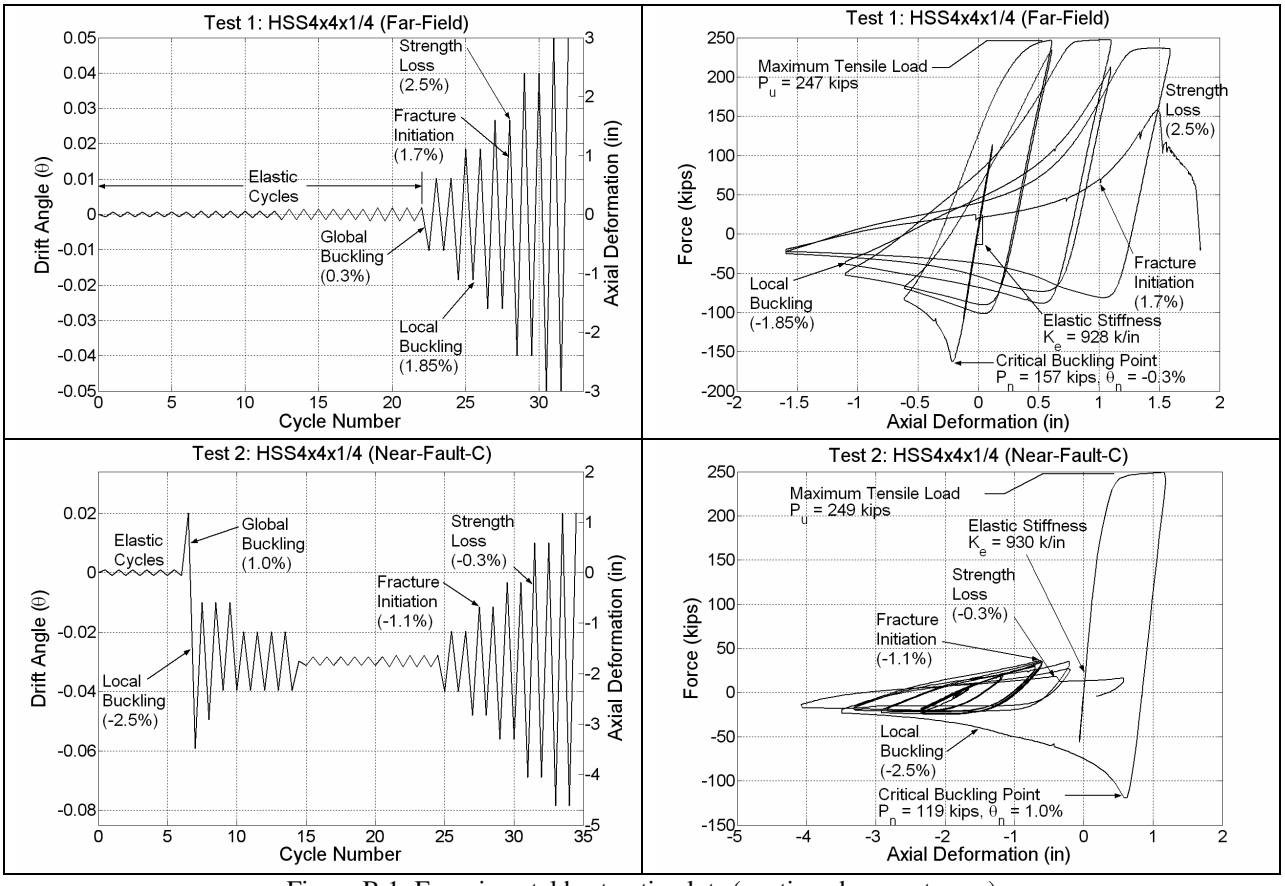


Figure B.1: Experimental hysteretic plots (continued on next page)

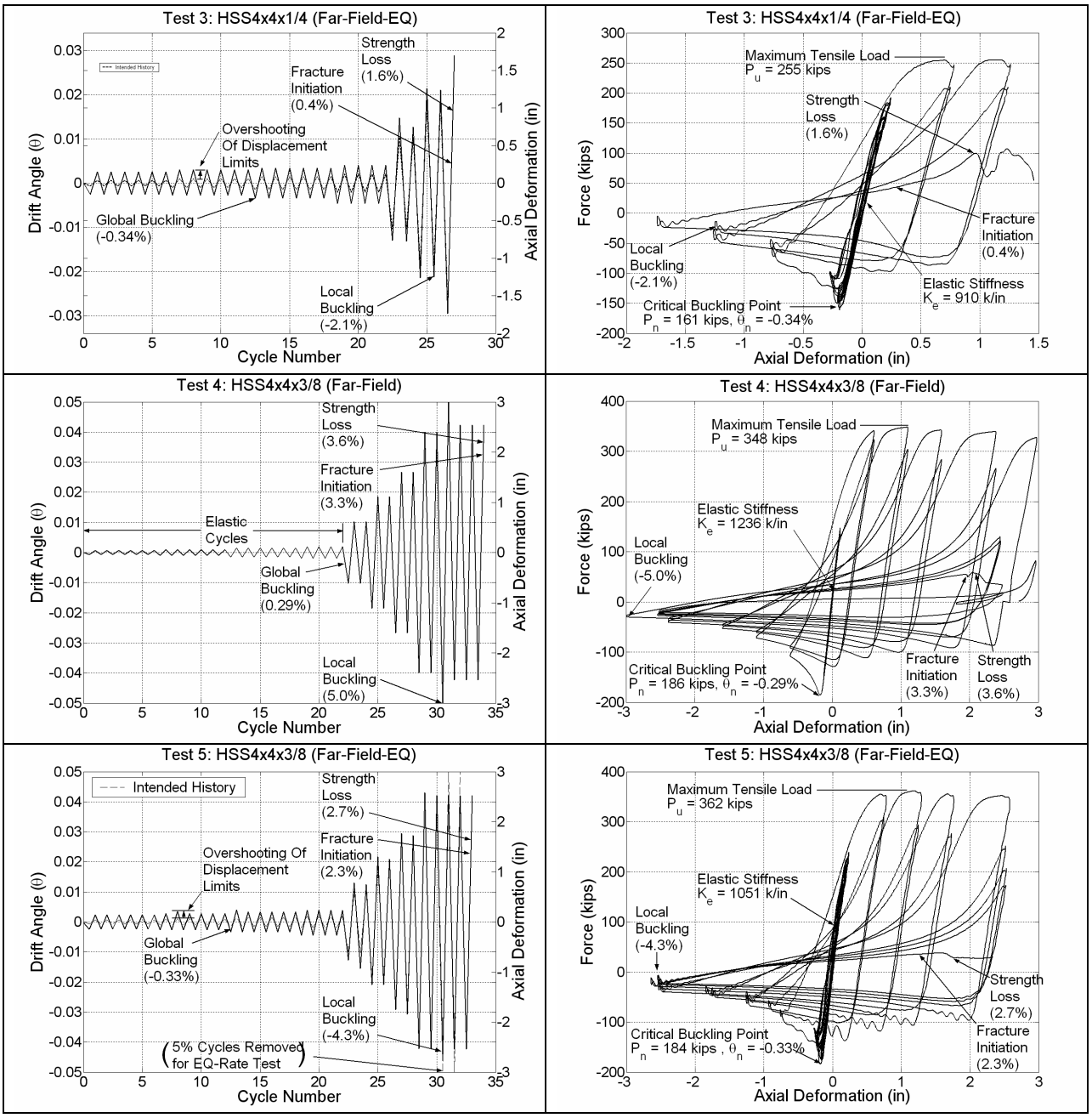


Figure B.1: Experimental hysteretic plots (continued)

 

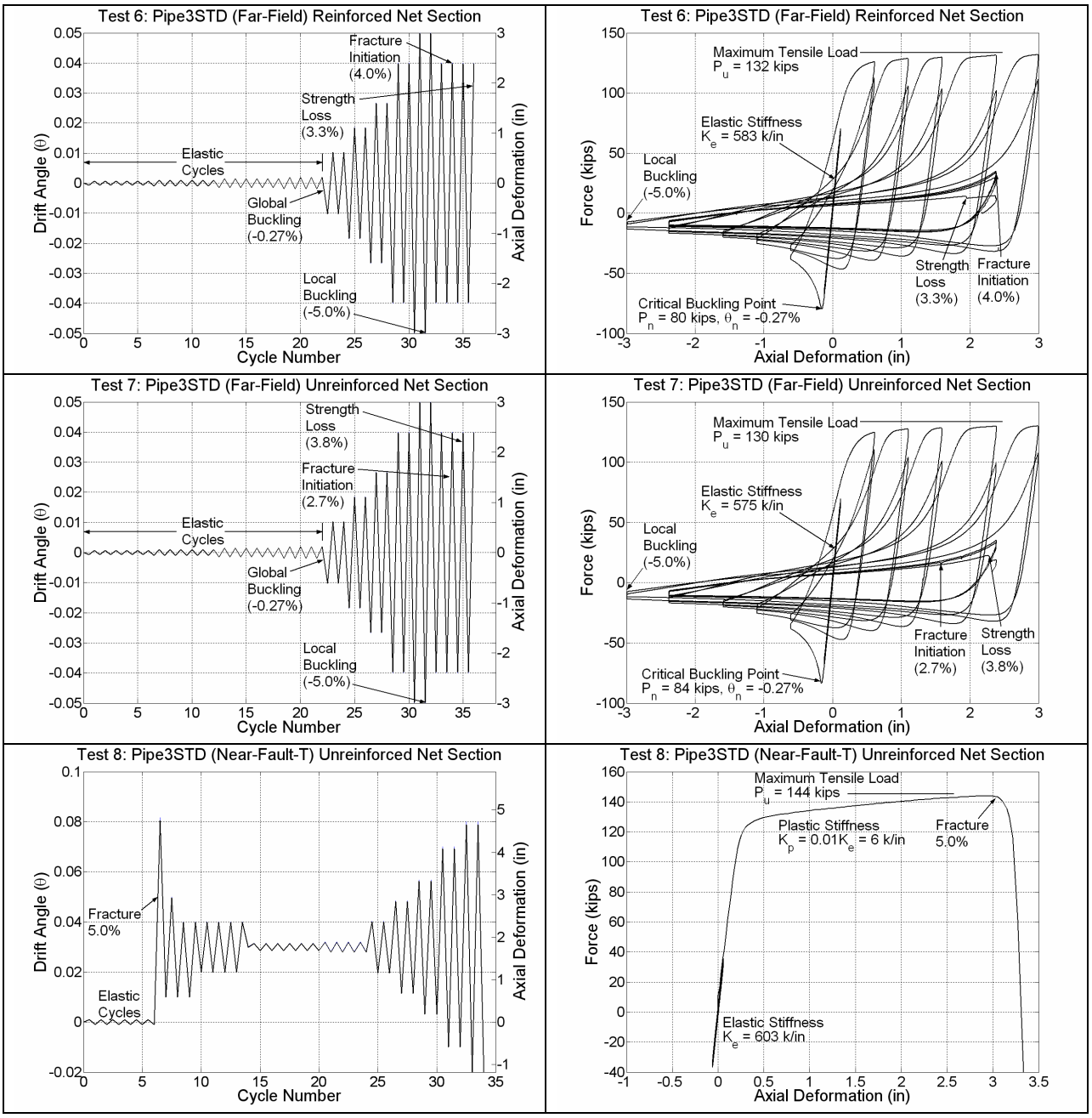


Figure B.1: Experimental hysteretic plots (continued)

 

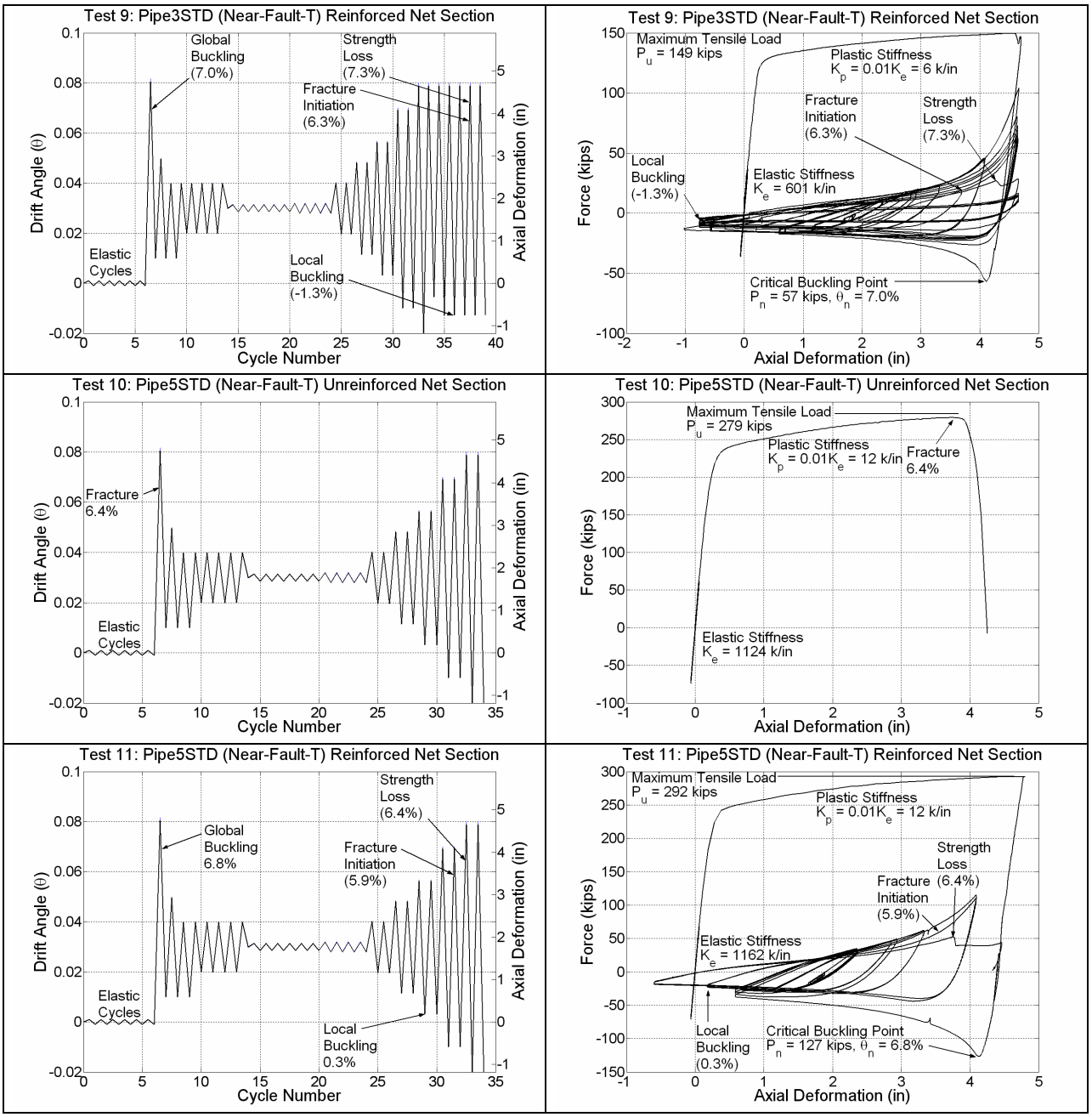


Figure B.1: Experimental hysteretic plots (continued)

 

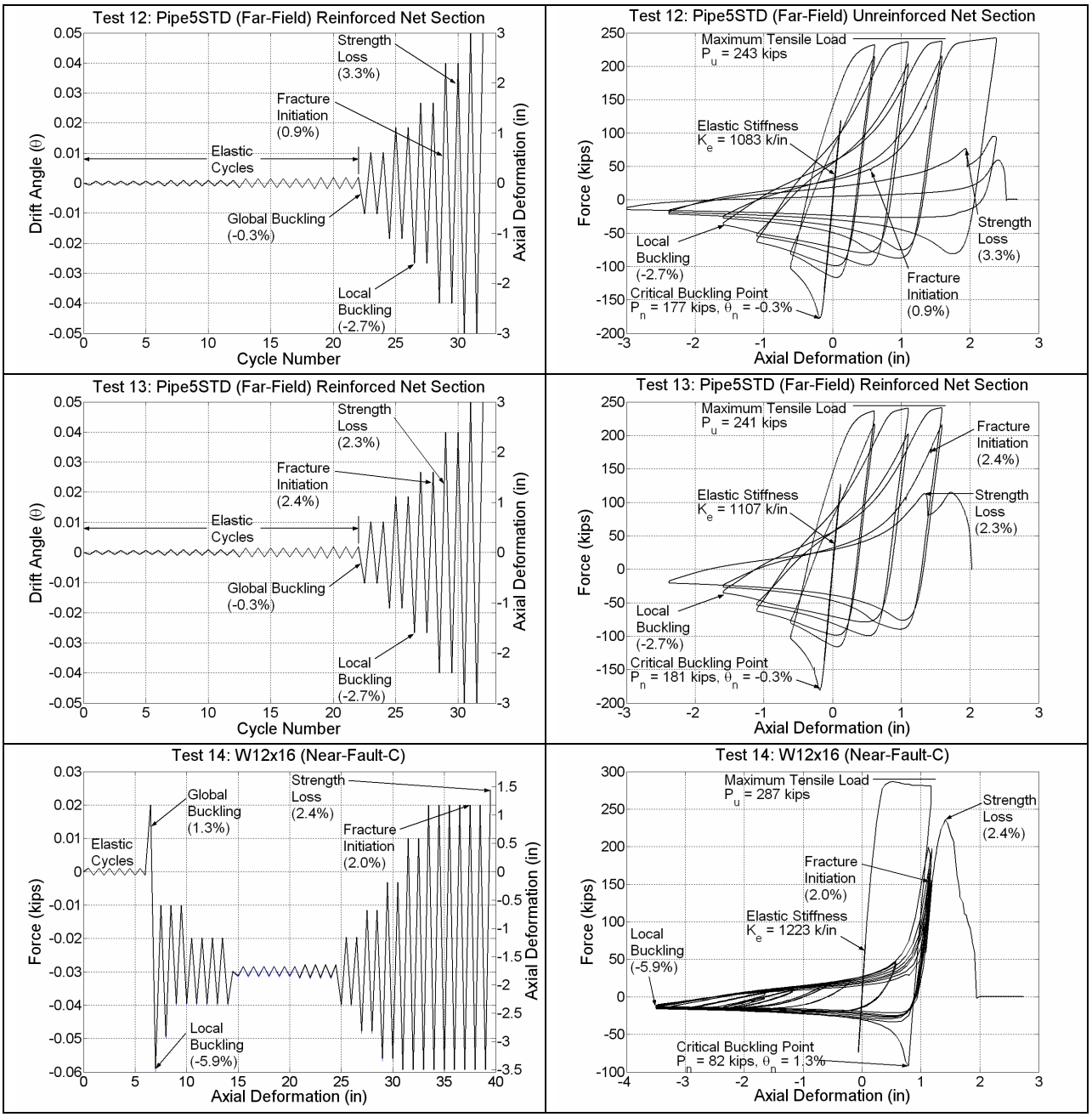


Figure B.1: Experimental hysteretic plots (continued)

 

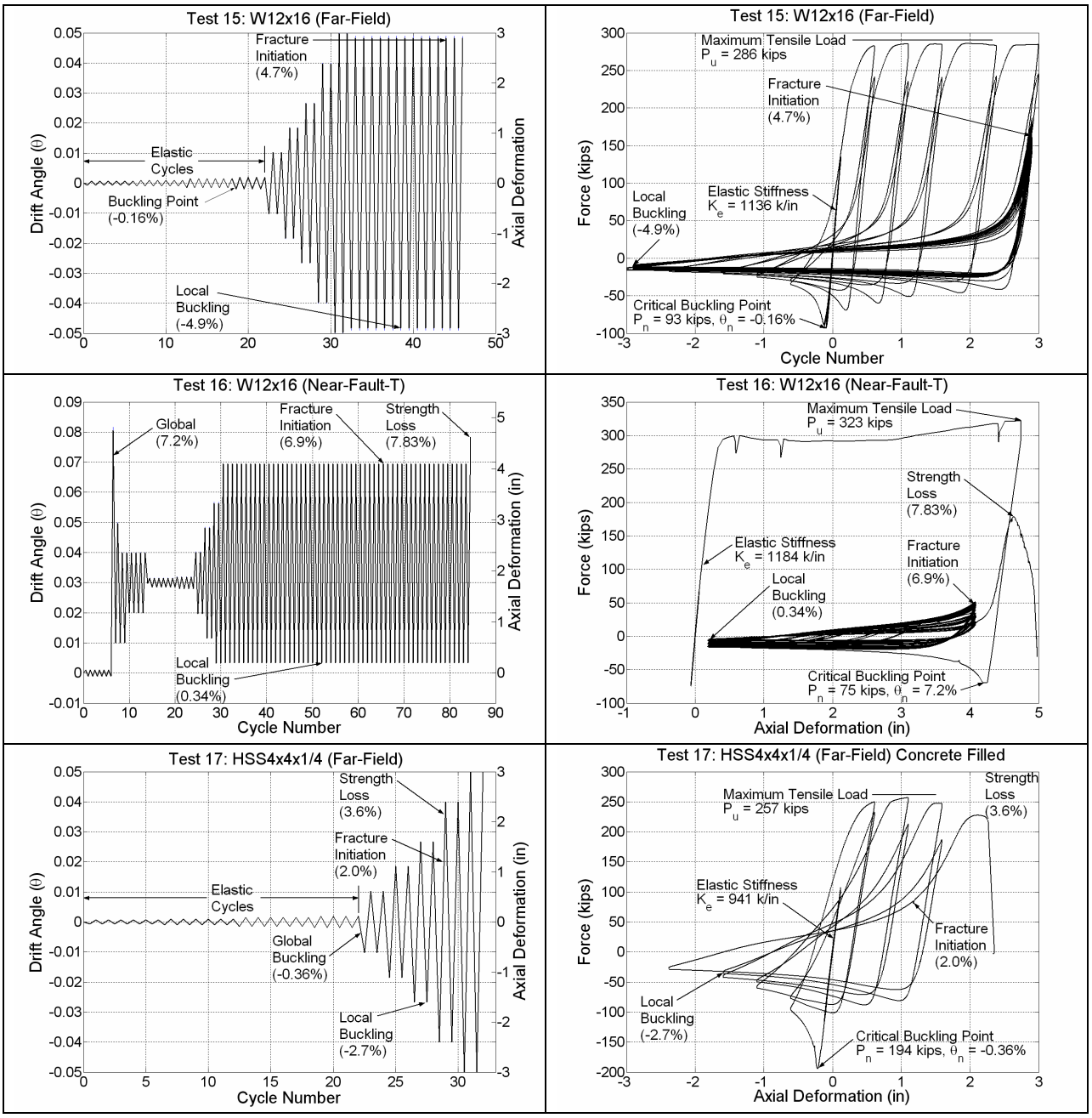


Figure B.1: Experimental hysteretic plots (continued)

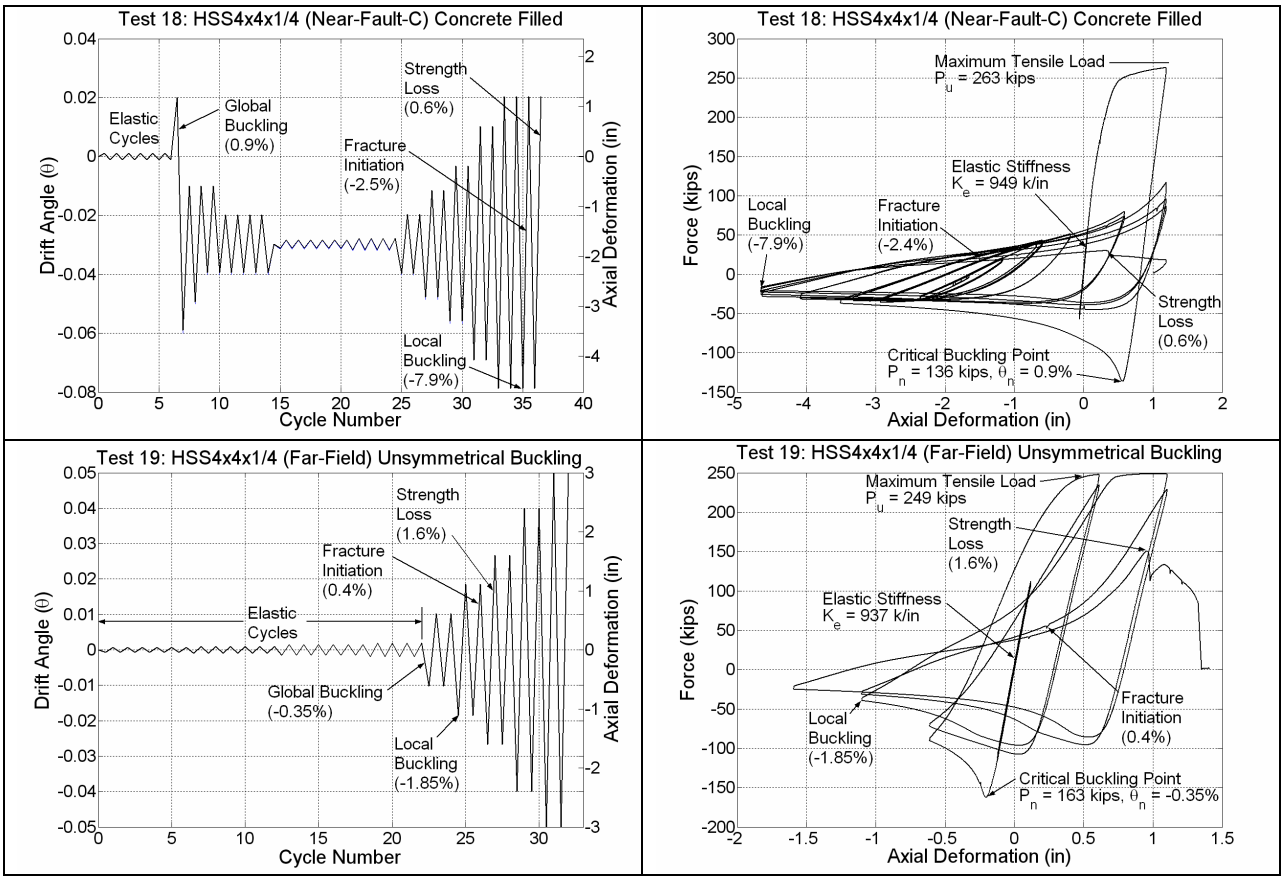


Figure B.1: Experimental hysteretic plots (continued)

Figure B.2 shows the tension and compression backbone curves for the experimental braces. The tension envelope consists of an elastic, perfectly-plastic response while the compression envelope transitions to a buckling response after the elastic region. These backbone curves can be used in conjunction with cyclic hysteretic rules (Ikeda and Mahin, 1986) to simulate response.

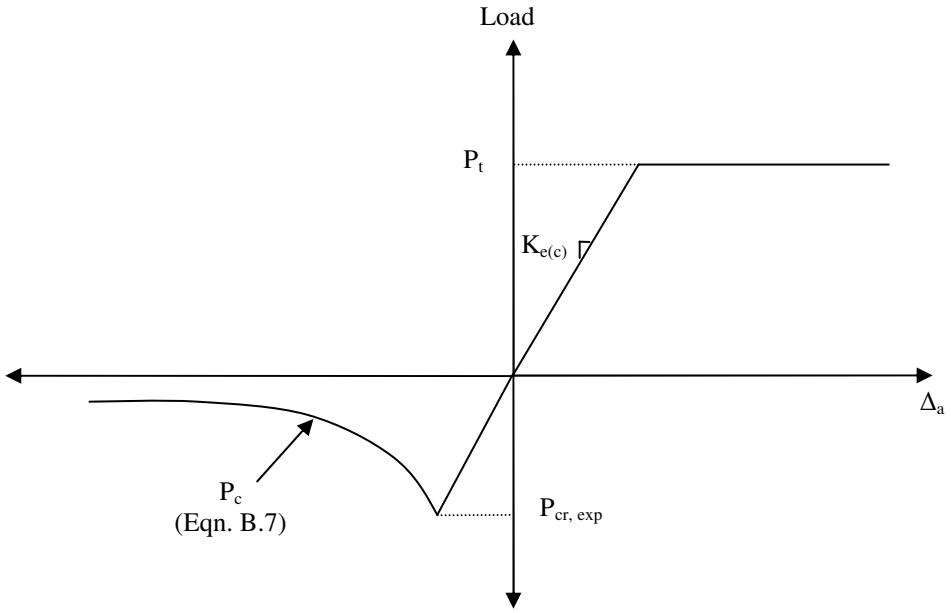


Figure B.2: Schematic backbone curves

The tension backbone of a brace is conveniently described with an elastic, perfectly-plastic response. This is shown in Eq. B.1.

$$K_{e(c)}\Delta_a,\ \Delta_a \le \frac{P_t}{K_{e(c)}}$$
$$P_t,\ \Delta_a > \frac{P_t}{K_{e(c)}} \qquad \text{(B.1)}$$

Given the material and geometric properties of the brace, the variables in the above bilinear formulation can be computed with relationships described by Eq. B.2. Note that the maximum expected force can be determined by $R_yF_yA_g$ or $R_tF_uA_g$. The latter is the more conservative estimate, while $R_yF_y$ can be more accurate for statistically average steels and typical design level events. See section 4.4 for a more detailed explanation.

$$K_{e(c)} = \frac{A_g E}{L_B} \qquad P_t = \begin{cases} R_t F_u A_g \\ R_y F_y A_g \end{cases} \qquad \text{(B.2)}$$

The compression backbone was derived by assuming a concentrated plastic hinge at the midpoint of the brace and fundamental geometric relationships explained below. Figure B.3

 

shows a schematic of a buckling compression strut with initial length between hinge locations, $L_B$, axial displacement, $\Delta$, lateral displacement, $\delta$, rotation angle, $\varphi$, and plastic moment, $M_P$.

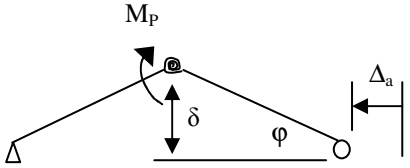


Figure B.3: Buckling schematic

The relationship between the rotation and axial displacement can be given by the following relationship assuming small angles:

$$\Delta_a = L_B(1-\cos\varphi) \approx \frac{L_B\varphi^2}{2} \tag{B.3}$$

The relationship between rotation of the central plastic hinge and lateral displacement can be given by:

$$\varphi = \frac{2\delta}{L_B} \tag{B.4}$$

The plastic capacity (assuming elastic, perfectly-plastic behavior) of the hinge can be expressed with the plastic modulus of the section, Z, and can be related to the lateral displacement through equilibrium:

$$P_c\delta = M_P = R_Y F_Y Z \tag{B.5}$$

From equations B.4 and B.5 it can be shown that:

$$P_c = R_Y F_Y Z\sqrt{\frac{2}{L_B\Delta_a}} \tag{B.6}$$

An initial imperfection, $\Delta_0$, is assumed for the axial strut, which is a function of the maximum expected compressive load, $P_{cr,exp}$. This requires the backbone to transition from the elastic region to buckling behavior at the maximum compressive load.

$$P_c = -\begin{cases} K_{e(c)}\Delta_a, \ \Delta_a \le \dfrac{P_{cr,\max}}{K_{e(c)}} \\ R_y F_Y Z \sqrt{\dfrac{2}{L_B(\Delta_a - \Delta_0)}}, \ \Delta_a > \dfrac{P_{cr,\max}}{K_{e(c)}} \end{cases}$$

where, (B.7)

$$\Delta_0 = \Delta_n - \frac{2(R_y F_Y Z)^2}{P_{cr,\max}^2 L_B} = \frac{P_{cr,\max} L_B}{A_g E} - \frac{2(R_y F_Y Z)^2}{P_{cr,\max}^2 L_B}$$

$P_{cr,exp}$ is the nominal capacity of a compression member and is determined by amplifying $F_y$ by the $R_y$ factor as illustrated in the example in section 2.6.3, while $\Delta_n$ is $P_{cr,exp}/K_{e(c)}$. The tension ($P_t$) and compression backbones ($P_c$) are compared to three experimental force deformation curves for the HSS4x4x1/4, Pipe3STD, and W12x16 subjected to the far-field loading history (Figures B.3 through B.5). The figures show that the nominal compression capacities are lower than the experimental buckling loads; however, the subsequent compression cycles are predicted quite accurately. The $R_tF_uA_g$ prediction for the HSS is quite accurate, while for the Pipe3STD and W12x16 the envelope overestimates the actual behavior. As discussed in section 4.4, tensile demand prediction is a complex issue and there are several alternatives to using the $R_tF_uA_g$ formulation ($R_yF_yA_g$ is also shown in Figures B.3 – B.5).

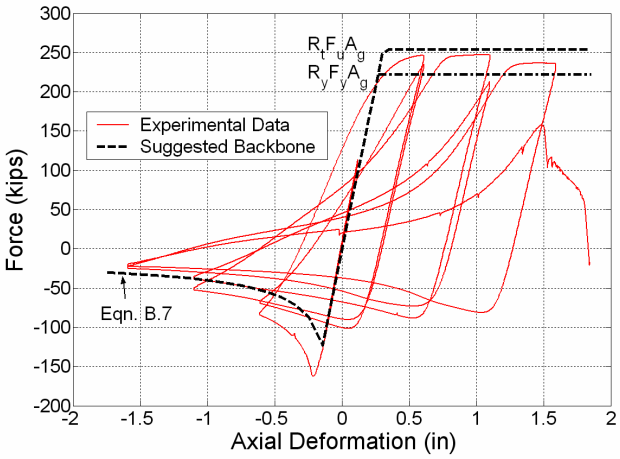


Figure B.3: Comparison of backbones to Test #1 data

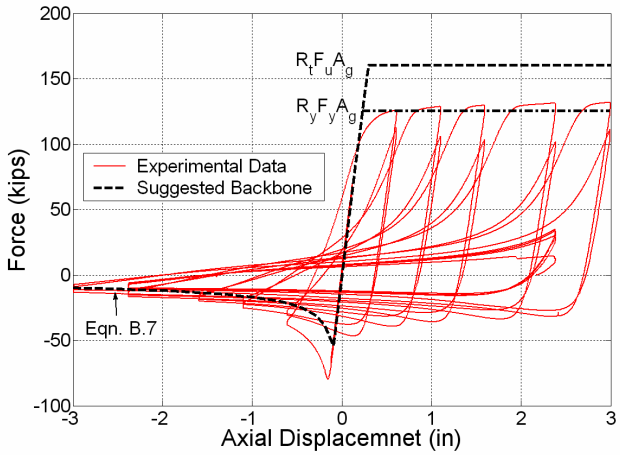


Figure B.4: Comparison of backbones to Test #7 data

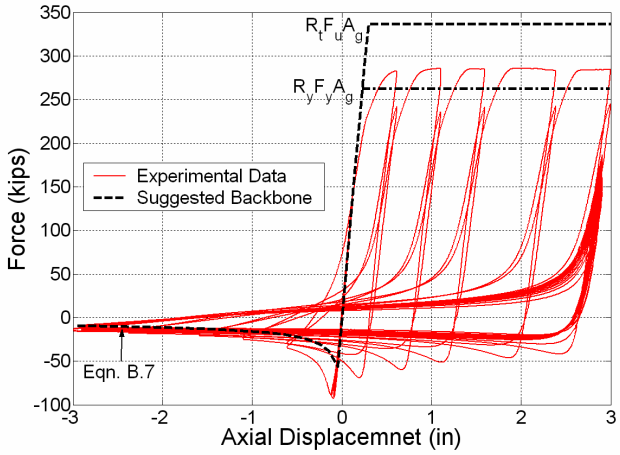


Figure B.5: Comparison of backbones to Test #15 data

 

# References


ABAQUS. 1998. User's Manual, Version 5.8, Hibbitt, Karlsson, and Sorensen, Inc., Providence, RI.

AISC. 2001. Load and Resistance Factor Design Specification for Structural Steel Buildings, 3rd ed. American Institute of Steel Construction, Chicago, IL.

AISC. 2005. Seismic Provisions for Structural Steel Buildings, American Institute of Steel Construction Inc., Chicago, IL.

American Society of Civil Engineers. 2005. ASCE-7-05: Minimum Design Loads for Buildings and Other Structures, Reston, VA.

Anderson, T.L. 1995. *Fracture Mechanics*, 2nd Ed., CRC Press, Boca Raton, FL.

Astaneh-Asl, A., Goel, S.C., and Hanson, R.D. 1985. "Cyclic Out-of-Plane Buckling of Double-Angle Bracing." *Journal of Structural Engineering* 111, 1135-1153.

Astaneh-Asl, A. 1998. "Seismic Behavior and Design of Gusset Plates." *SteelTIPS Series*, Structural Steel Education Council, Moraga, CA.

ATC, 1992. ATC-24, Guidelines for Cyclic Seismic Testing of Components of Steel Structures, Applied Technology Council.

Gupta, A., and Krawinkler, H. 1999. "Prediction of seismic demands for SMRFs with ductile connections and elements." *SAC Background Document, Report No. SAC/BD-99/06*.

Herman, D., Johnson, S., Lehman, D. and Roeder, C. 2006. "Improved seismic design of special concentrically braced frames." *Proc. 8th US Nat. Conf. on Earthquake Eng*., San Francisco, CA, Paper No. 1356.

Ikeda, K. and Mahin. S.A. 1986. "Cyclic Response of Steel Braces." *Journal of Structural Engineering* 112 (2), 342-361.

Kanvinde, A., and Deierlein, G.G. 2004. "Micromechanical Simulation of Earthquake Induced Fractures in Steel Structures." *Blume Center TR145*, http://blume.stanford.edu, Stanford University, Stanford, CA.

Koteski, N., Packer, J.A., and Puthli, R.S. 2005. "Notch Toughness of Internationally Produced Hollow Structural Sections." *Journal of Structural Engineering* 131 (2), 279-286.


 

Krawinkler, H., Gupta, A., Median, R., and Luco N. 2000. "Loading histories for seismic performance testing of SMRF Components and Assemblies." *SAC Joint Venture, Report No. SAC/BD-00/10.*

Liu, J., Sabelli, R., Brockenbrough, R.L., and Fraser, T. P. 2005. "Expected Yield and Tensile Strength Ratios for Determination of Expected Member Capacity in the 2005 AISC Seismic Provisions." *In Review.*

Liu, Z., and Goel, S. C. 1988. "Cyclic Load Behavior of Concrete-Filled Tubular Braces." *Journal of Structural Engineering* 114 (7), 1488-1506.

Open System for Earthquake Engineering Simulation (OpenSEES). 2005. Pacific Earthquake Engineering Research Center, http://opensees.berkeley.edu/. University of California, Berkeley.

Rice, J. R., and Tracey, D.M. 1969. "On the ductile enlargement of voids in triaxial stress fields." *Journal of the Mechanics and Physics of Solids* 17, 201-217.

Salmon, C. G., and Johnson, J. E. 1996. *Steel Structures, Design and Behavior*, 4th ed. New York: HaperCollins.

Shaback, B., and Brown, T. 2003. "Behavior of square hollow structural steel braces with end connections under reversed cyclic axial loading." *Candian Journal of Civil Engineering* 30, 745-753.

Tang, X., and Goel S. C. 1989. "Brace Fractures and Analysis of Phase I Structures." *Journal of Structural Engineering* 115 (8), 1960-1976.

Tremblay, R. 2000. "Influence of brace slenderness on the seismic response of concentrically braced steel frames." *Behavior of steel structures in seismic areas: proceedings of the 3rd International Conference STESSA*. 527-534.

Tremblay, R. 2001. "Seismic behavior and design of concentrically braced steel frames." *AISC Engineering Journal,* 3rd qtr., 148–166.

Tremblay, R. 2002. "Inelastic seismic response of steel bracing members." *Journal of Construction Steel Research* 58, 665-701.

Tremblay, R., Archambault, M-H., and Filiatrault, A. 2003. "Seismic Response of Concentrically Brace Steel Frames Made with Rectangular Hollow Bracing Members." *Journal of Structural Engineering* 129 (12), 1626-1636.

Uriz, P., and Mahin, S.A. 2004. "Seismic Performance Assessment of Concentrically Braced Steel Frames." *Proceedings of the 13th World Conference on Earthquake Engineering*

Whitmore, R.E. 1950. “Experimental Investigation of Stresses in Gusset Plates.” Masters Thesis, University of Tennessee Engineering Experiment Station Bulletin No. 16.

Yang, F., and Mahin, S.A. 2005. “Limiting Net Section Fracture in Slotted Tube Braces.” *Steel Tips Series*, Structural Steel Education Council, Moraga, CA.

 

## *About the Authors…*

***Benjamin V. Fell is a graduate research assistant at the University of California at Davis studying in the structural engineering and structural mechanics group within the civil engineering department. His Ph.D. dissertation deals with using micromechanical based modeling to predict fracture and fatigue in large-scale steel structures. This is a NEESR project funded by the National Science Foundation.***

***He is a winner of the 2005 AISC/SSEC Fellowship and was recognized nationally in CENews magazine as one of four "star students" in 2003. After graduating with highest honors from Rensselaer Polytechnic Institute with a Bachelors of Science he transferred to Stanford University where he received his Masters of Science in structural engineering.***

***He can be reached at:***

***Benjamin V. Fell***
***2021 Engineering III***
***University of California***
***Davis, CA 95616***
***(530) 752-3448***
***bvfell@ucdavis.edu***
***http://cee.engr.ucdavis.edu/faculty/kanvinde/KRP/Ben/index.html***

***Andrew T. Myers is a graduate research assistant at Stanford University working under Dr. Gregory Deierlein. He graduated with a bachelor's degree in Civil Engineering from Johns Hopkins University in 2004 and plans to continue at Stanford to pursue his Ph.D. in Structural Engineering. His research focuses on the fracture of steel and weld metal subjected to earthquake loads.***

***He can be reached at:***

***Andrew T. Myers***
***Blume Earthquake Engineering Center***
***Stanford University***
***439 Panama at Duena – Building 540***
***Stanford CA 94305-4020***
***(650)725-0381***
***atmyers@stanford.edu***
***http://www.stanford.edu/~amyers1***

***XiangYang Fu is a graduate research assistant at the University of California at Davis studying in the structural engineering and structural mechanics group within the civil engineering department.***

***He graduated from Tsinghua University in China with a bachelor's degree in structural engineering and got his master's degree in Washington State University. His Ph.D. dissertation deals with using micromechanical based modeling to predict fracture and fatigue in large-scale steel connections.***

***He can be reached at:***

***XiangYang Fu***
***2013 Engineering III***
***University of California***
***Davis, CA 95616***
***(530)754-6424***
***xfu@ucdavis.edu***

*Gregory G. Deierlein, Ph.D., P.E., is a professor of structural engineering at the Stanford University where he is the director of the John A. Blume Earthquake Engineering Research Center.*

*His research and professional interests focus on improving the structural design of buildings, bridges, and other constructed facilities. His research includes both computational and experimental techniques with emphasis on the development and application of nonlinear analysis of structural limit states, characterization of structural material and component behavior, performance-based engineering for earthquake and fire hazards, finite element simulation of ductile crack initiation in steel structures, design and behavior of composite steel-concrete structures.*

*Deierlein is active in several national technical and specification committees, including the American Institute of Steel Construction's Specification Committee, the Structural Stability Research Council, the Earthquake Engineering Research Institute, and the ASCE and ACI Committees on Composite Construction. Deierlein presently serves as Deputy Director for Research of the Pacific Earthquake Engineering Research (PEER) center, whose mission is to develop a comprehensive methodology and enabling technologies for performance-based earthquake engineering. Prior to joining Stanford University in 1998, Deierlein was on the faculty at Cornell University and worked as a structural engineer with the firm of Leslie E. Robertson and Associates in New York.*
*He can be reached at:*

*Gregory G. Deierlein, Ph.D., P.E.*
*Blume Earthquake Engineering Center, Room 118*
*Stanford University*
*Stanford, CA 94305-4020*
*ggd@stanford.edu*
*http://www.stanford.edu/group/strgeo/People/deierlein.html*

*Amit M. Kanvinde, Ph.D., is an assistant professor of structural engineering at the University of California at Davis.*

*His research focuses on fracture and fatigue of steel structures, nonlinear structural analysis and design, earthquake engineering and performance of steel structures. His work includes experimental techniques as well as theoretical and analytical techniques especially micromechanics-based modeling and computational mechanics. He currently leads a NEESR project investigating the ultra-low cycle fatigue fracture of steel structures.*

*Prior to joining UC Davis as an Assistant Professor in 2004, Kanvinde obtained his Masters and Doctoral degrees at Stanford University, and a Bachelors degree from the Indian Institute of Technology, Mumbai, India.*

*He can be reached at:*

*Amit M. Kanvinde, Ph.D.*
*3139 Engineering III*
*University of California*
*Davis, CA 95616*
*(530) 752-2605*
*kanvinde@ucdavis.edu*
*http://cee.engr.ucdavis.edu/faculty/kanvinde/*

## List of Published Steel TIPS Reports*

---

May 05: Design of Shear Tab Connections for Gravity and Seismic Loads, by Abolhassan Astaneh-Asl.
April 05: Limiting Net Section Fracture in Slotted Tube Braces, by Frances Yang and Stephen Mahin.
July 04: Buckling Restrained Braced Frames, by Walterio A. Lopez and Rafael Sabelli.
May 04: Special Concentric Braced Frames, by Michael Cochran and William Honeck.
Dec. 03: Steel Construction in the New Millenium, by Patrick M. Hassett.
August 2002: Cost Consideration for Steel Moment Frame Connections, by Patrick M. Hassett and James J. Putkey.
June 02: Use of Deep Columns in Special Steel Moment Frames, by Jay Shen, Abolhassan Astaneh-Asl and David McCallen.
May '02: Seismic Behavior and Design of Composite Steel Plate Shear Walls, by Abolhassan Astaneh-Asl.
Sept. '01: Notes on Design of Steel Parking Structures Including Seismic Effects, by Lanny J. Flynn, and Abolhassan Astaneh-Asl.
Jun '01: Metal Roof Construction on Large Warehouses or Distribution Centers, by John L. Mayo.
Mar. '01: Large Seismic Steel Beam-to-Column Connections, by Egor P. Popov and Shakhzod M.Takhirov.
Jan '01: Seismic Behavior and Design of Steel Shear Walls, by Abolhassan Astaneh-Asl.
Oct. '99: Welded Moment Frame Connections with Minimal Residual Stress, by Alvaro L. Collin and James J. Putkey.
Aug. '99: Design of Reduced Beam Section (RBS) Moment Frame Connections, by Kevin S. Moore, James O. Malley and Michael D. Engelhardt.
Jul. '99: Practical Design and Detailing of Steel Column Base Plates, by William C. Honeck & Derek Westphal.
Dec. '98: Seismic Behavior and Design of Gusset Plates, by Abolhassan Astaneh-Asl.
Mar. '98: Compatibility of Mixed Weld Metal, by Alvaro L. Collin & James J. Putkey.
Aug. '97: Dynamic Tension Tests of Simulated Moment Resisting Frame Weld Joints, by Eric J. Kaufmann.
Apr. '97: Seismic Design of Steel Column-Tree Moment-Resisting Frames, by Abolhassan Astaneh-Asl.
Jan. '97: Reference Guide for Structural Steel Welding Practices.
Dec. '96: Seismic Design Practice for Eccentrically Braced Frames (Based on the 1994 UBC), by Roy Becker & Michael Ishler.
Nov. '95: Seismic Design of Special Concentrically Braced Steel Frames, by Roy Becker.
Jul. '95: Seismic Design of Bolted Steel Moment-Resisting Frames, by Abolhassan Astaneh-Asl.
Apr. '95: Structural Details to Increase Ductility of Connections, by Omer W. Blodgett.
Dec. '94: Use of Steel in the Seismic Retrofit of Historic Oakland City Hall, by William Honeck & Mason Walters.
Dec '93: Common Steel Erection Problems and Suggested Solutions, by James J. Putkey.
Oct. '93: Heavy Structural Shapes in Tension Applications.
Mar. '93: Structural Steel Construction in the '90s, by F. Robert Preece & Alvaro L. Collin.
Aug. '92: Value Engineering and Steel Economy, by David T. Ricker.
Oct. '92: Economical Use of Cambered Steel Beams.
Jul. '92: Slotted Bolted Connection Energy Dissipaters, by Carl E. Grigorian, Tzong-Shuoh Yang & Egor P. Popov.
Jun. '92: What Design Engineers Can Do to Reduce Fabrication Costs, by Bill Dyker & John D. Smith.
Apr. '92: Designing for Cost Efficient Fabrication, by W.A. Thornton.
Jan. '92: Steel Deck Construction.
Sep. '91: Design Practice to Prevent Floor Vibrations, by Farzad Naeim.
Mar. '91: LRFD-Composite Beam Design with Metal Deck, by Ron Vogel.
Dec. '90: Design of Single Plate Shear Connections, by Abolhassan Astaneh-Asl, Steven M. Call and Kurt M. McMullin.
Nov. '90: Design of Small Base Plates for Wide Flange Columns, by W.A. Thornton.
May '89: The Economies of LRFD in Composite Floor Beams, by Mark C. Zahn.
Jan. '87: Composite Beam Design with Metal Deck.
Feb. '86: UN Fire Protected Exposed Steel Parking Structures.
Sep. '85: Fireproofing Open-Web Joists & Girders.
Nov. '76: Steel High-Rise Building Fire.

The Steel TIPS are available at website: www.steeltips.org and can be downloaded for a nominal fee for personal use courtesy of the California Field Iron Workers Administrative Trust.

# STRUCTURAL STEEL EDUCATIONAL COUNCIL

**P.O. Box 6190**
**Moraga, CA 94570**
**Tel. (925) 631-1313**
**Fax. (925) 631-1112**

**Fred Boettler, Administrator**

**Steel TIPS may be viewed and downloaded for a nominal fee at**
**www.steeltips.org**

## Participating Members of SSEC

ABOLHASSAN ASTANEH-ASL, Ph.D., P.E.; UNIV. OF CALIFORNIA, BERKELEY
FRED BREISMEISTER, P.E.: STROCAL, INC.
MICHAEL COCHRAN, S.E.; BRIAN L. COCHRAN ASSOCIATES
RICH DENIO; KPFF CONSULTING ENGINEERS
JEFFREY EANDI, P.E.; EANDI METAL WORKS, INC.
PATRICK M. HASSETT, S.E.: HASSETT ENGINEERING, INC.
JOHN KONECHNE, P.E.; CALIFORNIA ERECTORS, INC.
DERRICK LIND; LIFTECH CONSULTANTS, INC.
WALTERIO LOPEZ; S.E.; RUTHERFORD/CHEKENE
BRETT MANNING, S.E.
LARRY MCLEAN, MCLEAN STEEL, INC.
KEVIN MOORE; CETUS CONSULTING INC.
JAY MURPHY; MURPHY PACIFIC CORPORATION
RICHARD PERSONS; U.S. STEEL
JAMES J. PUTKEY, P.E.; CONSULTING CIVIL ENGINEER
STEVE THOMPSON; SME STEEL CONTRACTORS

**Funding for this publication provided by the California Field Iron Workers Administrative Trust.**